Neutral Bremsstrahlung Emission in Xenon Unveiled

C. A. O. Henriques,[1,†] P. Amedo,[2] J. M. R. Teixeira,[1] D. González-Díaz,[2] C. D. R. Azevedo,[3] A. Para,[4] J. Martín-Albo,[5] A. Saa Hernandez,[2] J. J. Gómez-Cadenas,[6,7,‡] D. R. Nygren,[8,‡] C. M. B. Monteiro[1,*] C. Adams,[9] V. Álvarez,[10] L. Arazi,[11] I. J. Arnquist,[12] K. Bailey,[9] F. Ballester,[10] J. M. Benlloch-Rodríguez,[6,5] F. I. G. M. Borges,[13] N. Byrnes,[8] S. Cárcel,[5] J. V. Carrión,[5] S. Cebrián,[14] E. Church,[12] C. A. N. Conde,[13] T. Contreras,[15] G. Díaz,[2] J. Díaz,[5] M. Diesburg,[4] J. Escada,[13] R. Esteve,[10] R. Felkai,[11,16,5] A. F. M. Fernandes,[1] L. M. P. Fernandes,[1] P. Ferrario,[6,7] A. L. Ferreira,[3] E. D. C. Freitas,[1] J. Generowicz,[6] S. Ghosh,[15] A. Goldschmidt,[17] R. Guenette,[15] R. M. Gutiérrez,[18] J. Haefner,[15] K. Hafidi,[9] J. Hauptman,[19] J. A. Hernando Morata,[2] P. Herrero,[6] V. Herrero,[10] Y. Ifergan,[11,16] B. J. P. Jones,[8] M. Kekic,[2,5] L. Labarga,[20] A. Laing,[8] P. Lebrun,[4] N. López-March,[10,5] M. Losada,[18] R. D. P. Mano,[1] A. Martínez,[5,6] M. Martínez-Vara,[5] G. Martínez-Lema,[5,2,§] A. D. McDonald,[8] F. Monrabal,[6,7] F. J. Mora,[10] J. Muñoz Vidal,[5,6] P. Novella,[5] B. Palmeiro,[2,5] J. Pérez,[21] M. Querol,[5] A. B. Redwine,[11] J. Renner,[2,5] J. Repond,[9] S. Riordan,[9] L. Ripoll,[22] Y. Rodríguez García,[18] J. Rodríguez,[10] L. Rogers,[8] B. Romeo,[6,21] C. Romo-Luque,[5] F. P. Santos,[13] J. M. F. dos Santos,[1] A. Simón,[11] C. Sofka,[23,‖] M. Sorel,[5] T. Stiegler,[23] J. F. Toledo,[10] J. Torrent,[6] A. Usón,[5] J. F. C. A. Veloso,[3] R. Webb,[23] R. Weiss-Babai,[11,¶] J. T. White,[23,**] K. Woodruff,[8] and N. Yahlali[5]

(NEXT Collaboration)

[1]*LIBPhys, Physics Department, University of Coimbra, Rua Larga, 3004-516 Coimbra, Portugal*
[2]*Instituto Gallego de Física de Altas Energías, Universidade de Santiago de Compostela,*
Campus sur, Rúa Xosé María Suárez Núñez, s/n, Santiago de Compostela, E-15782, Spain
[3]*Institute of Nanostructures, Nanomodelling and Nanofabrication (i3N), Universidade de Aveiro,*
22 Campus de Santiago, 3810-193 Aveiro, Portugal
[4]*Fermi National Accelerator Laboratory, Batavia, Illinois 60510, USA*
[5]*Instituto de Física Corpuscular (IFIC), CSIC and Universitat de València,*
Calle Catedrático José Beltrán, 2, Paterna, E-46980, Spain
[6]*Donostia International Physics Center (DIPC), Paseo Manuel Lardizabal, 4,*
Donostia-San Sebastian, E-20018, Spain
[7]*Ikerbasque, Basque Foundation for Science, Bilbao, E-48013, Spain*
[8]*Department of Physics, University of Texas at Arlington, Arlington, Texas 76019, USA*
[9]*Argonne National Laboratory, Argonne, Illinois 60439, USA*
[10]*Instituto de Instrumentación para Imagen Molecular (I3M), Centro Mixto CSIC-Universitat Politècnica de València, Camino de Vera s/n, Valencia, E-46022, Spain*
[11]*Nuclear Engineering Unit, Faculty of Engineering Sciences, Ben-Gurion University of the Negev,*
P.O.B. 653, Beer-Sheva, 8410501, Israel
[12]*Pacific Northwest National Laboratory (PNNL), Richland, Washington 99352, USA*
[13]*LIP, Department of Physics, University of Coimbra, 3004-516 Coimbra, Portugal*
[14]*Centro de Astropartículas y Física de Altas Energías (CAPA), Universidad de Zaragoza,*
Calle Pedro Cerbuna, 12, Zaragoza, E-50009, Spain
[15]*Department of Physics, Harvard University, Cambridge, Massachusetts 02138, USA*
[16]*Nuclear Research Center Negev, Beer-Sheva, 84190, Israel*
[17]*Lawrence Berkeley National Laboratory (LBNL), 1 Cyclotron Road, Berkeley, California 94720, USA*
[18]*Centro de Investigación en Ciencias Básicas y Aplicadas, Universidad Antonio Nariño, Sede*
Circunvalar, Carretera 3 Este No. 47 A-15, Bogotá, Colombia
[19]*Department of Physics and Astronomy, Iowa State University,*
12 Physics Hall, Ames, Iowa 50011-3160, USA
[20]*Departamento de Física Teórica, Universidad Autónoma de Madrid,*
Campus de Cantoblanco, Madrid, E-28049, Spain
[21]*Laboratorio Subterráneo de Canfranc, Paseo de los Ayerbe s/n,*
Canfranc Estación, E-22880, Spain
[22]*Escola Politècnica Superior, Universitat de Girona,*
Avenida Montilivi, s/n, Girona, E-17071, Spain

[23]*Department of Physics and Astronomy, Texas A&M University,*
College Station, Texas 77843-4242, USA

We present evidence of non-excimer-based secondary scintillation in gaseous xenon, obtained using both the NEXT-White time projection chamber (TPC) and a dedicated setup. Detailed comparison with first-principle calculations allows us to assign this scintillation mechanism to neutral bremsstrahlung (NBrS), a process that is postulated to exist in xenon that has been largely overlooked. For photon emission below 1000 nm, the NBrS yield increases from about 10^{-2} photon/e^- cm^{-1} bar^{-1} at pressure-reduced electric field values of 50 V cm^{-1} bar^{-1} to above 3×10^{-1} photon/e^- cm^{-1} bar^{-1} at 500 V cm^{-1} bar^{-1}. Above 1.5 kV cm^{-1} bar^{-1}, values that are typically employed for electroluminescence, it is estimated that NBrS is present with an intensity around 1 photon/e^- cm^{-1} bar^{-1}, which is about 2 orders of magnitude lower than conventional, excimer-based electroluminescence. Despite being fainter than its excimeric counterpart, our calculations reveal that NBrS causes luminous backgrounds that can interfere, in either gas or liquid phase, with the ability to distinguish and/or to precisely measure low primary-scintillation signals (S1). In particular, we show this to be the case in the "buffer" region, where keeping the electric field below the electroluminescence threshold does not suffice to extinguish secondary scintillation. The electric field leakage in this region should be mitigated to avoid intolerable levels of NBrS emission. Furthermore, we show that this new source of light emission opens up a viable path toward obtaining S2 signals for discrimination purposes in future single-phase liquid TPCs for neutrino and dark matter physics, with estimated yields up to 20–50 photons/e^- cm^{-1}.

DOI: [10.1103/PhysRevX.12.021005](https://doi.org/10.1103/PhysRevX.12.021005)   Subject Areas: Astrophysics, Particles and Fields

I. INTRODUCTION

Xenon time projection chambers (TPCs) with optical readout are increasingly applied to rare event detection in the important fields of astrophysics and particle physics, including dark matter searches [1–5] and in studies of neutrino physics such as double-beta decay [6–10], double-electron capture [11], and neutrino detection [12,13].

All xenon optical TPCs are based on the remarkable scintillation properties of this element, which responds to ionizing radiation emitting copious light in the vacuum ultraviolet (VUV), "second continuum" region. While a value around 172 nm has been measured for the secondary scintillation wavelength in gaseous xenon [14–16], a value

*Corresponding author.
cristinam@uc.pt
†Corresponding author.
henriques@uc.pt
‡NEXT Co-spokesperson.
§Present address: Weizmann Institute of Science, Israel.
‖Present address: University of Texas at Austin, USA.
¶On leave from Soreq Nuclear Research Center, Yavneh, Israel.
**Deceased.

of 178 nm was measured for the liquid xenon (LXe) primary scintillation (see, e.g., the review papers [17,18] and references therein). A more recent measurement quotes a value of 175 nm [19] for the LXe primary scintillation, a number that is gaining acceptance within the LXe community. The width of the emission is 10–15 nm.

Through the years, xenon primary and secondary scintillation have been studied in detail. Primary scintillation has been studied in solid and liquid xenon [20–25] and in the gas phase [26–30] for different types of interactions, while secondary scintillation promoted by electron impact has been studied mainly in the gas phase (Refs. [31–34], and references therein). To the best of our knowledge, only a few studies are presented in the literature for secondary scintillation in LXe (e.g., Refs. [35,36]). Xenon secondary scintillation produced in electron avalanches of modern micropatterned electron multipliers [37–39], as well as in dedicated scintillation-based structures [40,41], has been studied in the gas phase. In parallel to these investigations, detailed microscopic simulation packages have been introduced [42,43].

In all these studies, it is assumed that secondary scintillation is solely due to VUV emission from excimers created in a three-body collision of two neutral atoms and one excited atom produced by electron impact, the so-called electroluminescence (EL) mechanism. A recent review can be found in Ref. [44]. Nevertheless, more than 50 years ago, evidence of a scintillation mechanism distinct from EL was presented, accompanying electron transport in xenon [45]. The authors of Ref. [45] attribute this light

emission to neutral bremsstrahlung (NBrS), postulating its presence in all noble gases. In contrast to EL, NBrS occurs in the visible wavelength range and is also present for electron energies below the xenon excitation threshold (8.315 eV; see Ref. [43] and references therein). Only relative values for NBrS intensity are presented as a function of the pressure-reduced electric field, i.e., the electric field divided by the gas pressure E/p, in two different datasets with trends that are not in agreement with each other. This work remained largely unknown by the scientific community, and the NBrS emission in noble elements was subsequently mostly ignored.

NBrS is produced by ionization electrons when these are scattered on neutral atoms. Unlike the primary mechanism for EL production, the emission wavelength of NBrS ranges from the UV to the near-infrared region depending on the electron energy. It, therefore, depends on E/p. NBrS is, thus, expected to be the dominant scintillation mechanism for subexcitation electrons, competing with electroluminescence when electrons have energies around the xenon excitation threshold.

Very recent studies reveal NBrS emission in Ar TPCs [46–48]. This process could explain, for instance, the differences observed between the Ar secondary scintillation yield measured in a double-phase TPC [46,47] and that obtained in a gas proportional scintillation counter (GPSC) operated around normal temperature and pressure conditions [49]. NBrS was found to be important for Ar double-phase TPC operation, and its impact and relevance are being investigated within the Darkside Collaboration [50,51].

At low electron energies, the NBrS intensity can be shown to be proportional to the elastic electron-atom cross section [46], which is a universal interaction mechanism during electron drift in gases. As dark matter TPCs are pushing their sensitivities down to single-photon detection to be capable of covering light dark matter in the sub-GeV region as well as neutrino detection [12,13,52], it is important to investigate potential sources of photon emission taking place along the electron drift in both conversion or drift and EL regions in TPCs, as well as in the TPC buffer regions between the high-voltage electrodes and the grounded electrodes located in front of the photosensor planes.

In this work, we present unambiguous identification of NBrS emission in xenon TPCs and discuss its relevance in the context of rare event search experiments. We perform independent measurements, first using the NEXT-White (NEW) TPC [53], presently the largest optical high-pressure xenon (HPXe) TPC in operation, and second in a smaller GPSC-type detector [33,54], where the effect could be isolated and studied in greater detail. We provide a quantitative assessment of the NBrS emission yield as a function of the reduced electric field, supported by a predictive theoretical model of this light-emission process, which describes the experimental data very well.

In Sec. II, the theory of NBrS is briefly summarized, forming a basis for the simulation tools developed to describe this mechanism. In Sec. III A, we briefly describe the NEXT-White TPC and present evidence for a scintillation mechanism occurring at electric field intensities below the gas EL threshold; in Sec. III B, we describe the experimental setup used for measuring efficiently and under controlled conditions the xenon scintillation below the xenon EL threshold and the methodology that is used to analyze this scintillation. Section IV presents our experimental results and the validation of the simulation model, along with a discussion of the impact of NBrS emission on the LXe and HPXe TPCs developed for rare event detection. The general conclusions are presented in Sec. V, and the discussion of the uncertainties associated with the scintillation measurements are discussed in the Appendix.

II. NEUTRAL BREMSSTRAHLUNG

The interaction of an electron with the dipole field of a neutral atom or molecule can lead to radiative photon emission by analogy with the familiar case of nuclear bremsstrahlung [55–58]. From the kinematical point of view, the process is allowed, since the atomic recoil enables conservation of energy and momentum that would otherwise be impossible. We refer to this process as NBrS. It is a well-known phenomenon in plasma physics [59], and its inverse process i-NBrS governs the opacity of dense media to photons with energies below the atomic and molecular transitions [55].

Noble atoms, in particular, despite having no permanent dipole, can interact electromagnetically by virtue of their induced dipole moment or polarizability α, in the presence of external fields: For a given atomic number Z and charge e, the interaction potential as a function of distance r behaves asymptotically as

$$V(r) \simeq -\frac{1}{2} Z^2 e^2 \frac{\alpha}{r^4}. \tag{1}$$

NBrS can be studied starting from Fermi's golden rule, which allows calculating the transition probability between the "quasifree" states of the impinging and scattered electron in the presence of a weak perturbation (for details, see Ref. [58]). This leads to the fundamental expression for the emission spectrum of NBrS expressed as a differential cross section per unit of frequency [56]:

$$\frac{d\sigma}{d\nu} = \frac{8\pi e^2 \nu^3 m_e^2 k_f}{3\hbar^3 c^3 k_i} |M|^2 \tag{2}$$

with m_e being the electron mass, ν the photon frequency, $\hbar$ the reduced Planck constant, c the speed of light, $\hbar k_{i(f)}$ the initial (final) electron momentum, and M a matrix element involving the two electron states:

$$|M|^2 \equiv |\langle \Psi_f | \vec{r} | \Psi_i \rangle|^2. \qquad (3)$$

In the case of a swarm of ionization electrons (e.g., released during the interaction of ionizing radiation), the NBrS rate can be readily obtained by averaging over all possible electron energies (following a probability distribution $dP/d\varepsilon$), as

$$\frac{dN_\gamma}{d\nu dt} = \int_0^\infty N \frac{d\sigma}{d\nu} v(\varepsilon) \frac{dP}{d\varepsilon} d\varepsilon \qquad (4)$$

with N being the number of atoms per unit volume and $v(\varepsilon)$ the energy-dependent electron velocity [$v(\varepsilon) = \hbar k_i/m_e$].

Given that measurements in the present work are integrated over all photon frequencies (wavelengths) and recalling the convenience of using the yield per unit path length for the studies of EL in gases, Eq. (4) leads to

$$
\begin{aligned}
Y \equiv \frac{dN_\gamma}{dz} &= \frac{1}{v_d} \int_{\nu_{\min}}^{\nu_{\max}} \frac{dN_\gamma}{d\nu dt} d\nu \\
&= \frac{1}{v_d} \int_{\nu_{\min}}^{\nu_{\max}} \int_0^\infty N \frac{d\sigma}{d\nu} v(\varepsilon) \frac{dP}{d\varepsilon} d\varepsilon d\nu \text{ [ph/cm]}, \qquad (5)
\end{aligned}
$$

where v_d is the drift velocity of the electron swarm. In experimental conditions, Eq. (5) needs to include the frequency-dependent geometrical $GE(\nu)$ and quantum $QE(\nu)$ efficiencies of the detection system (Fig. 2 for the setup used in this work). In order to estimate the electron energy distribution, either Boltzmann solvers or electron transport by Monte Carlo method could be applied. The latter are used in this work. In particular, the recently developed PYTHON-version PyBoltz [60] of the well-known Magboltz transport code [61] allows one to easily obtain this distribution from the energy prior to each electron collision following the technical implementation suggested in Ref. [46].

Finally, $|M|^2$ in Eq. (2) may be approximated with the first-order terms in a partial wave analysis. If taking those by analogy with hydrogen (to 1% accuracy, in that case [57]), the following simplified form can be obtained [56]:

$$|M|^2 = \frac{64\pi^2}{(k_i^2 - k_f^2)^4} [k_i^2 Q(k_f) + k_f^2 Q(k_i)], \qquad (6)$$

where M is already averaged over all angles of the emitted photon and summed over the polarization directions and Q refers to the elastic cross section. How the angular distribution of NBrS photons can still be obtained after performing the angular average in Eq. (6) in the case of an electron swarm is discussed below. For the sake of the following argument, we note that the reference coordinate system for the calculation leading to Eq. (6) is taken with the z axis aligned along the momentum of the incoming electron and with the atom at rest, as is customary. For swarm observables (i.e., obtained for many electrons), we use a reference coordinate system with the z axis aligned
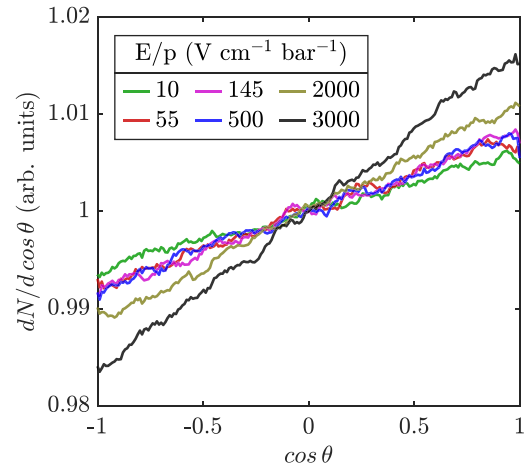

FIG. 1. Angular distributions ($dP/d\cos\theta$) obtained for the angle between the electron momentum vector and the direction of the electric field, prior to each collision, obtained with the transport code PyBoltz. For clearness, data are smoothed by a moving average.

along the electric field direction and with both species in movement (hereafter, "lab frame"), since calculations in this frame are of the most interest for comparison to experimental data. The kinematics of the NBrS interaction imposes that the scattering angle of the electron and photon are deterministically related; hence, these angles can be used interchangeably. Therefore, when in a swarm, the angular distribution of the emitted NBrS photons in the lab frame can be obtained from (i) the angular distribution of scattered photons (electrons) in the reference frame of the impinging electron and (ii) the angular distribution of the impinging electrons themselves relative to the electric field orientation in the lab frame. Thus, averaging over the scattered photon (electron) angles in the reference frame of the impinging electron, as done in Eq. (6), destroys essential information on the final angular distribution of NBrS photons in the lab frame, except if that could be established through an independent argument. In fact, the latter is the case. According to PyBoltz, the angular distribution of the impinging electrons prior to each collision, in the lab frame, is highly isotropic for the considered electric fields and pressures, deviating by less than 1% (Fig. 1). This small linear correction is expected from the first term of a Legendre expansion, corresponding to the well-known "two-term approximation" widely used in Boltzmann solvers when applied to pure noble gases. Thus, irrespective of the angular distribution of emitted photons relative to the electron momentum direction, the momentum distribution isotropy of the impinging electrons within the swarm leads to isotropic NBrS emission in the lab frame for all conditions studied in this work. This establishes an important result for the experimental study of NBrS in high-density media, substantially different from other bremsstrahlung emissions.
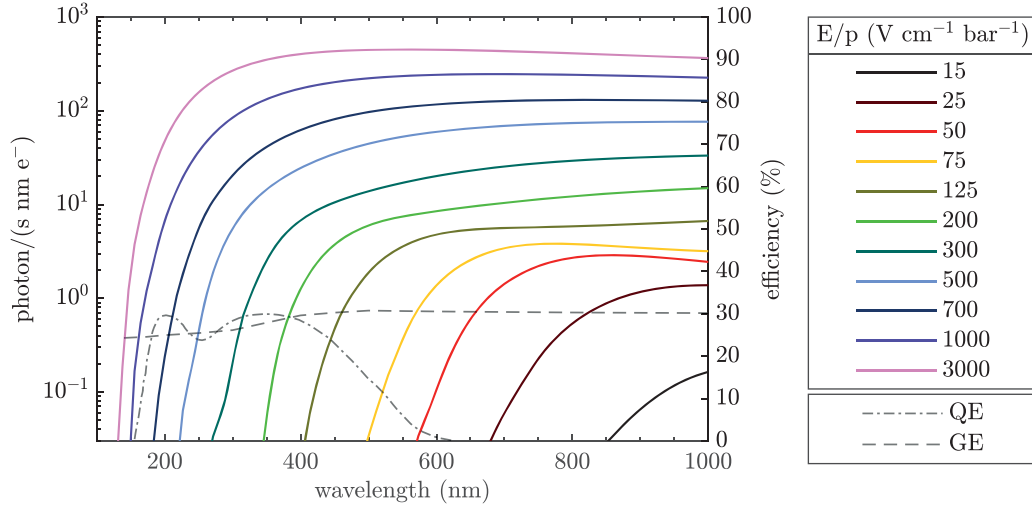
FIG. 2.   Computed NBrS emission rate as a function of the wavelength for different electric field values, using Eq. (7) with Q_m. The quantum efficiency of the PMT used for the main part of the measurements presented in this work is indicated by the dot-dashed line. The geometrical efficiency of the experimental setup, calculated with GEANT4 (see a description later in the text), is indicated by the dashed line.

Our final expression can be obtained by substituting Eq. (6) in Eq. (2) and recalling the relationships $\varepsilon_{i,f} = (\hbar^2/2m_e)k_{i,f}^2$, $h\nu = \varepsilon_i - \varepsilon_f$:

$$\frac{d\sigma}{d\nu} = \frac{8}{3}\frac{r_e}{c}\frac{1}{h\nu}\left(\frac{\varepsilon_i - h\nu}{\varepsilon_i}\right)^{1/2}$$
$$\cdot\,[\varepsilon_i \cdot Q_{(m)}(\varepsilon_i - h\nu) + (\varepsilon_i - h\nu) \cdot Q_{(m)}(\varepsilon_i)] \quad (7)$$

with $r_e = e^2/(m_e c^2)$ being the classical radius of the electron. This expression is discussed in Refs. [46,59] and is used hereafter. It must be noted that the calculation of the matrix element in Eq. (6) represents an approximation, and, indeed, independent arguments applied to the limit of low photon energy (i.e., $h\nu/\varepsilon_i < 1$; see, e.g., Ref. [62]) suggest that Q in Eq. (7) should be replaced by the momentum transfer cross section Q_m:

$$Q_m = \int_0^1 \frac{dQ}{d\cos\theta}(1 - \cos\theta)d\cos\theta, \quad (8)$$

θ being the angle between the electron momentum vector and the direction of the electric field.

For computation of "subthreshold" scintillation yields in Xe gas, Eq. (7) with either Q or Q_m provides very similar results after being inserted in Eq. (5) and numerically integrating over photon and electron energies. Later, it is shown that, despite simplifications of the theoretical treatment, either procedure reproduces to high accuracy the characteristic behavior of the scintillation yield as a function of the electric field. As an example, for the purpose of illustrating the main characteristics of the emission, the numerical evaluation of

$$\frac{dN_\gamma}{d\lambda dt} = \frac{d\nu}{d\lambda}\frac{dN_\gamma}{d\nu dt} \quad (9)$$

in Xe for different electric field values is given in Fig. 2.

III. EXPERIMENTAL SETUP AND METHODOLOGY

A. The NEXT-White detector

The NEXT Collaboration seeks to discover the neutrinoless double-beta ($0\nu\beta\beta$) decay of ^{136}Xe using a high-pressure xenon gas time projection chamber with EL amplification [63]. The unambiguous observation of $0\nu\beta\beta$ decay would prove lepton number violation and the Majorana nature of the neutrino. Xenon has no other long-lived radioactive isotopes that are expected to produce backgrounds to the double-beta decay of ^{136}Xe. The ^{136}Xe $Q_{\beta\beta}$ value is relatively high (approximately 2.5 MeV [64]), and the half-life of the $2\nu\beta\beta$ mode is in excess of 10^{21} yr [65,66]. Therefore, ^{136}Xe is an attractive isotope for $0\nu\beta\beta$ searches based on considerations of background mitigation.

At present, NEXT is operating the world's largest HPXe optical TPC, which is currently taking data at the Laboratorio Subterreneo de Canfranc (LSC) in the Spanish Pyrenees. The NEXT-White TPC (Fig. 3) is the first radiopure implementation of the NEXT TPC and deploys approximately 5 kg of xenon in an active cylindrical volume of approximately 53 cm length and approximately 40 cm in diameter, at a pressure of 10 bar. The energy measurement is provided by 12 Hamamatsu R11410-10 photomultiplier tubes (PMTs), having 31% area coverage and placed 130 mm from a transparent wire array cathode, which is held at negative high voltage. A 2D array (10-mm pitch) of 1792 SensL C-Series,
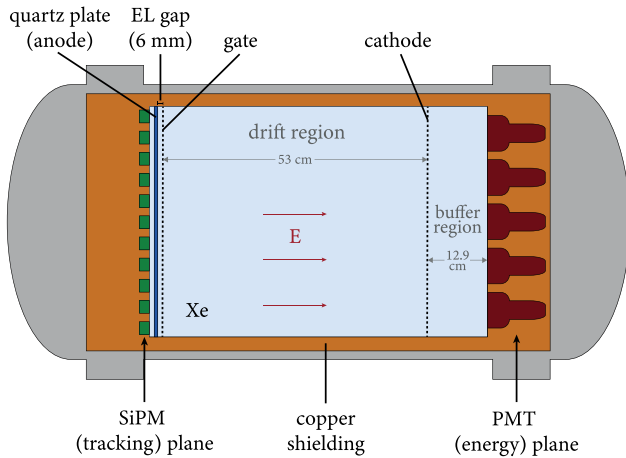
FIG. 3. Schematic of the EL-based TPC developed by the NEXT Collaboration for double-beta decay searches in ^{136}Xe, adapted from Ref. [67].

1-mm^2 silicon photomultipliers (SiPMs), placed a few millimeters behind the electroluminescence (EL) gap, is used for particle track reconstruction. The EL gap is approximately 6 mm thick and is defined by a stainless-steel mesh and a grounded quartz plate coated with indium tin oxide (ITO) and tetraphenyl butadiene (TPB) thin films. An electric field is established in the drift region defined by the cathode and the gate mesh, while the electric field in the EL region is defined by the mesh voltage.

Charged particles deposit energy in the conversion (drift) region, which is the sensitive volume of the detector, producing a track of ionized and excited xenon atoms. The VUV scintillation resulting from the deexcitation processes and from electron or ion recombination, called the primary scintillation or the S1 signal, provides the t_0 signal or the start-of-drift time stamp for the event. The ionization electrons are guided toward the EL region by the drift field whose value, around 40 V cm^{-1} bar^{-1}, is well below the xenon scintillation threshold. In the EL region, under the influence of an electric field with an intensity between the gas scintillation and the gas ionization thresholds, each electron attains from the electric field enough kinetic energy to excite but not ionize the xenon atoms. In the deexcitation processes, a large yield of secondary scintillation is released, the S2 signal, without charge avalanche formation.

The (x, y) positions of the electrons arriving at the EL region are determined by reading out the EL in the SiPM readout plane; the difference in time between the primary and the EL scintillation signals defines the z position at which the ionization event takes place. These parameters can be conveniently used for fiducializing events that occur close to the chamber boundaries that are likely to originate from radiogenic backgrounds.

The TPC is connected to a gas system through which the gaseous xenon is continuously purified via a hot getter (MonoTorr PS4-MT50-R from SAES). The TPC active volume is shielded by a 60-mm-thick ultrapure inner copper shell, and the sensor planes are mounted on pure copper plates 120 mm in thickness. The sensor planes and the active volume are enclosed in a pressure vessel constructed out of titanium-stabilized stainless-steel alloy ^{316}Ti. To reduce the background rate, the TPC is mounted inside a lead "castle" on a seismic platform in Hall A of LSC. The inner volume of the castle is flushed with radon-free air, having a ^{222}Rn content 4–5 orders of magnitude lower than the LSC Hall A air [68], from a radon abatement system by ATEKO A.S. This results in a measured Rn activity below 1.5 mBq m^{-3} in the air delivered to the lead castle [68]. The experimental setup is similar to that of the preceding study [69], and a comprehensive description of NEXT-White can be found in Ref. [53].

The amplification of primary ionization signals through EL results in both a higher signal-to-noise ratio [70,71], due to the additional gain of the photosensor, and lower statistical fluctuations when compared to charge avalanche multiplication [72]. The NEXT-White TPC demonstrates an energy resolution value below 1% FWHM [67] at the xenon $Q_{\beta\beta}$, while the best energy resolution achieved in a smaller (1 kg) prototype based on charge avalanche amplification extrapolates to 3% FWHM [73]. In addition, EL readout through photosensors electrically and mechanically decouples the amplification region from the readout, rendering the system more immune to electronic noise, radio-frequency pickup, and high-voltage issues. When compared to LXe-based TPCs, HPXe TPCs achieve better energy resolution and allow for an efficient discrimination of the rare event through its topological signature based on track topology analysis with the determination of Bragg peaks at the track ends [6,73–75]. The energy resolution (FWHM) reached in NEW TPC for 42, 662, and 2615 keV is 4.86% [69], 1.20%, and 0.91% [67], respectively, while for XENON1T TPC these resolutions are around or above 12%, 3%, and 2% [76], respectively, and are even higher for LUX, XENON100, PandaX-II, and EXO-200 TPCs (see Ref. [76] and references therein).

The energy (PMT) plane is used to trigger the detector, resorting to either the S1 or the S2 scintillation signal. Individual waveforms obtained in the energy plane, summed over all PMTs, e.g., Fig. 4, are selected and classified as "S1-like" or "S2-like." Events with a single identified S1 signal are selected, and the S2 peaks are divided into slices of 2 μs in width. Rebinning the SiPM waveforms to 2 μs slices constitutes the best trade-off between spatial reconstruction along the drift direction and SiPM signal-to-noise ratio for S2 signals: Signal-to-noise is worse for 1 μs slices, while spatial reconstruction starts to degrade for time slices well above 2 μs. The energies ε of the reconstructed deposition points along the track (x, y, z, and ε) are subsequently multiplied by two correction factors: one accounting for the geometrical (x, y)
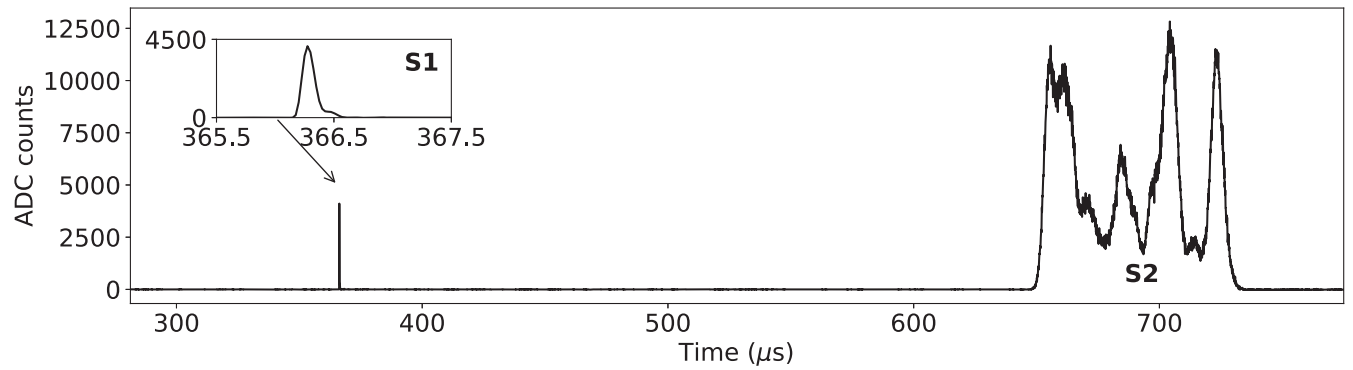
FIG. 4. Typical waveform, summed over all PMTs, for an event from ^{208}Tl gamma (2.6 MeV) photoelectric absorption. Signals S1 and S2 are highlighted (adapted from Ref. [67]).

dependence of the light collection over the EL plane and another one accounting for losses due to the finite electron lifetime caused by attachment to impurities. This second factor depends on both the drift length (z coordinate) and
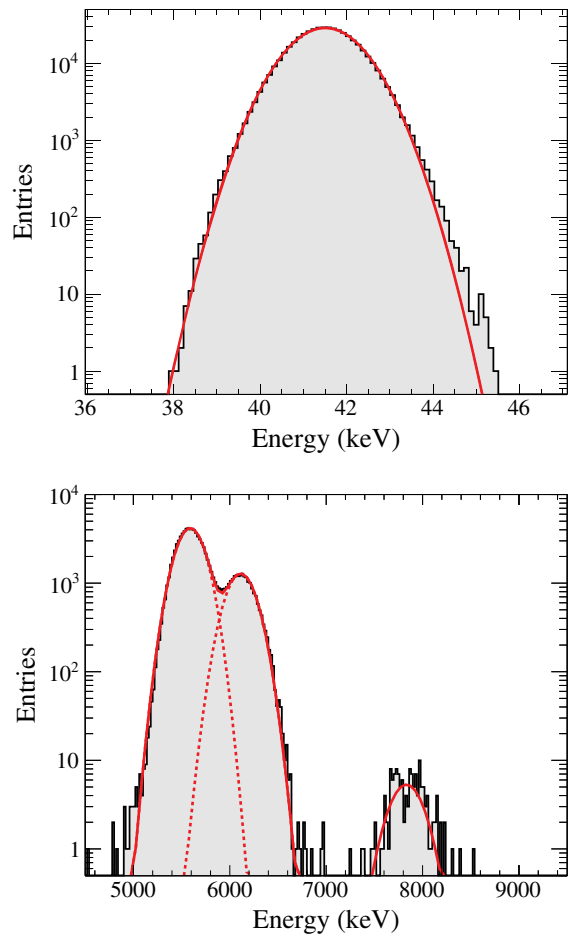

FIG. 5. Secondary scintillation (S2) spectra registered in the NEXT-White detector for ^{83m}Kr decays at 41.5 keV (top) and ^{222}Rn (5.590 MeV), ^{218}Po (6.112 MeV), and ^{214}Po (7.834 MeV) alphas (bottom), obtained at 1.7 and 0.62 kV cm^{-1} bar^{-1} in the EL region, respectively.

the location on the EL plane (x, y), since the electron lifetime varies in (x, y) as well due to the nonuniform distribution of impurities. Continuous detector calibration and monitoring are carried out with an ^{83m}Kr low-energy calibration source ensuring high-quality and properly calibrated low-background data [77].

Compared to extended MeV-electron tracks, both ^{83m}Kr events and α particles produce nearly pointlike energy depositions, and the (x, y, z) corrections are straightforward. An example of the energy spectra reconstructed in both cases is shown in Fig. 5. Circulating xenon through a cold getter [78] allows us to have a source of radon-induced alphas in the whole fiducial volume, at a rate of several hertz. Therefore, alpha-rich runs, particularly at the beginning of a new experimental campaign, may be used to characterize the detector, similar to the regular calibration performed with ^{83m}Kr. With this aim, in the first runs of 2017 a routine high-voltage scan at 7 bar is performed at a very low EL voltage in order not to saturate the PMTs using α events. Further analysis of the peak position of alpha
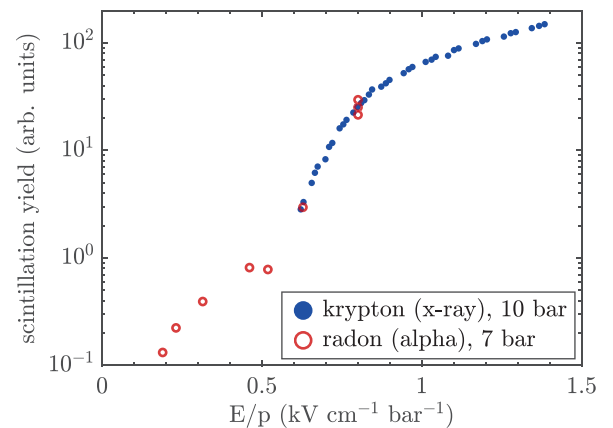

FIG. 6. Secondary scintillation (S2) measured for x rays (closed circles) and α particles (open circles) with the NEW-TPC. No corrections for the wavelength-shifting effect of the TPB, light collection, or quantum efficiency are applied.

particles from the Rn progeny and of ^{83m}Kr events suggests an excess of scintillation below the EL threshold, as shown in Fig. 6. The EL threshold is commonly defined as $-b/m$, where m and b are the slope and the y intercept, respectively, of a linear function fitted to the linear region of the EL yield as a function of E/p (see Ref. [32] and references therein). An EL threshold of approximately $0.71 \text{ kV cm}^{-1} \text{ bar}^{-1}$ is obtained from the data shown in Fig. 6. It is very significant that alpha particles can still be identified in the NEXT-White TPC for drift fields as low as $200 \text{ V cm}^{-1} \text{ bar}^{-1}$, due to the presence of this subthreshold emission. This observation motivates us to repeat the measurements under well-controlled conditions, with the goal of determining the origin of this phenomenon with minimal ambiguity and excluding instrumental artifacts.

B. The driftless GPSC

For detailed studies of subthreshold secondary scintillation, we employ a "driftless" GPSC that, unlike regular GPSCs used in Ref. [72] for x-ray spectroscopy, does not feature a drift region (Fig. 7). Such a configuration is optimal for scintillation studies, since it avoids potential limitations due to electronegative impurities or charge recombination at typical values of the drift field and does not require any optimization of the primary electron transfer to the EL region, which is usually done by means of a mesh.

In our chamber, the 2.45-cm-thick EL region is delimited by a Kapton window (8 mm in diameter, aluminized on the inner side, mounted on a stainless-steel holder), the cathode, and the quartz PMT window, which has on its outer surface a vacuum-evaporated chromium grid (100-μm-thick strips with 1000-μm spacing), the anode, electrically connected to the photocathode pin. The PMT model is EMI D676QB with a diameter of 52 mm and a spectral sensitivity in the range of 155–625 nm, thereby avoiding the use of any wavelength shifter. The PMT is epoxied to a hollow Macor disk of about 10 cm in diameter, which is also epoxied to the lower part of the detector that is made out of stainless steel and welded to the gas circulation tubing. The detector is filled with pure Xe at a pressure of 1.24 bar (estimated temperature of about 300 K), and the gas is being continuously purified through hot getters (SAES St-707). This concept is described in detail in previous studies [33,54].

A large number of primary electrons is required to reach an experimental sensitivity acceptable to the foreseen subthreshold scintillation. Therefore, the detector is irradiated with alpha particles from a collimated ^{241}Am source. A 5-μm Mylar film is placed between the source and the Kapton window to reduce the alpha particle penetration into the gas volume, in order for the initial charge distribution to be almost pointlike and distant from the anode. The tracks of the alpha particles are simulated using the software package "Stopping and Range of Ions in Matter" (SRIM) [79]. A mean energy deposition of 1.70 ± 0.22 MeV is estimated, and the distribution of ionization electrons is found to have a longitudinal spread of 1.64 ± 0.17 mm centered at a depth of 2.56 ± 0.27 mm, with a transverse spread of 1.5 ± 0.2 mm.

The PMT output is connected directly to a WaveRunner 610Zi oscilloscope from LeCroy, with a sampling rate of up to 10 GS s^{-1}, using the 50-Ω dc coupling to match the cable impedance. Since the light emission studied in this

1 - kapton window
2 - grid evaporated on PMT
3 - radioactive source
4 - lead collimator
5 - to gas purifier

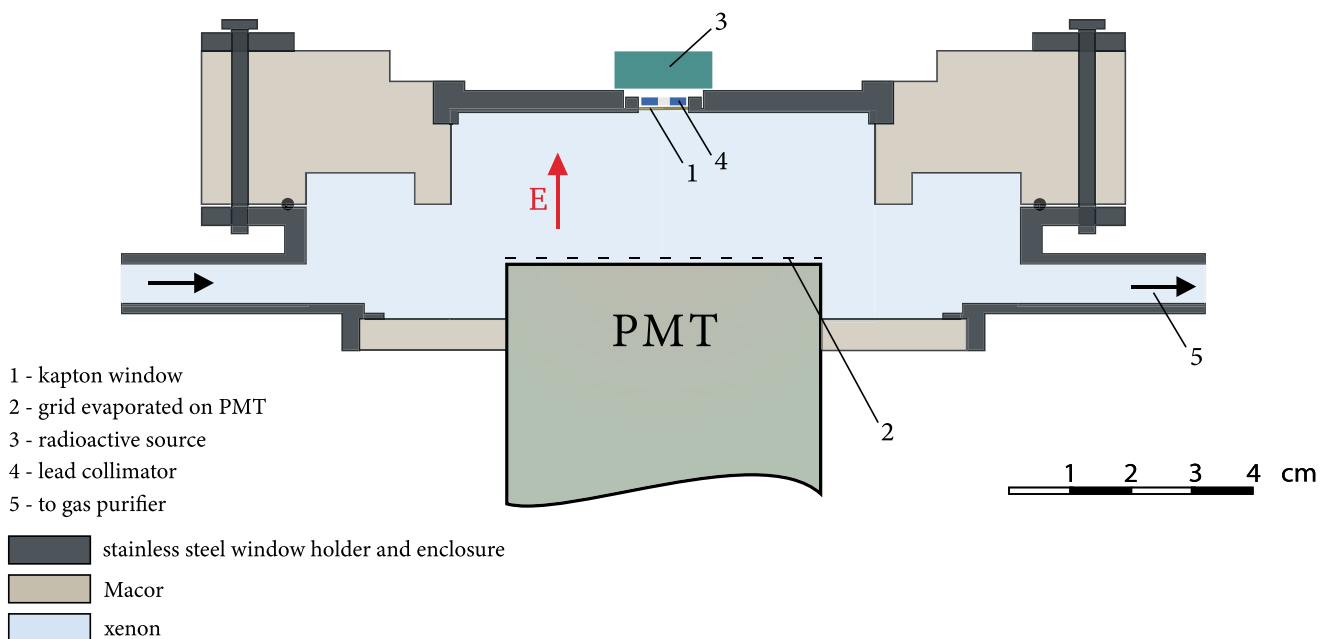■ stainless steel window holder and enclosure

■ Macor

■ xenon

FIG. 7.   Schematic of the driftless GPSC used in this work, adapted from Ref. [33].
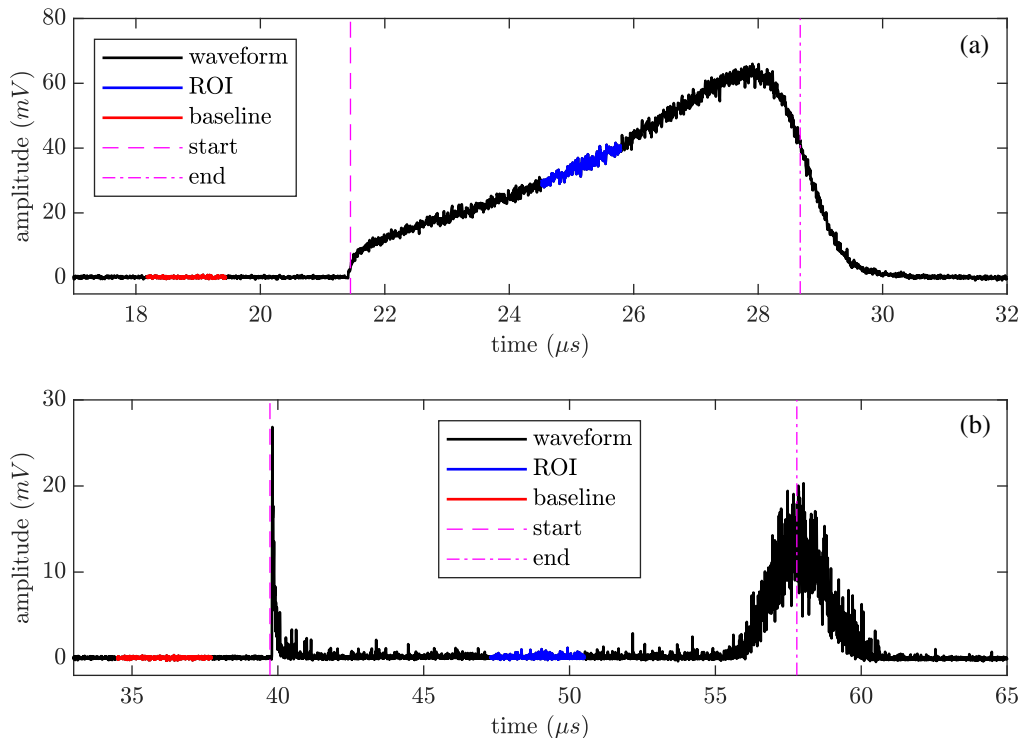
FIG. 8.   Typical driftless GPSC waveforms obtained for an E/p value of 1.5 kV cm^{-1} bar^{-1}, higher than the EL threshold (a) and for an E/p of 320 V cm^{-1} bar^{-1}, lower than the EL threshold (b). The start and end of event are represented by vertical lines. The regions chosen to determine the NBrS and EL (ROI) are indicated in blue.

work covers a wide range of intensities, the PMT bias voltage is adjusted between 650 and 1400 V to reach optimal signal-to-noise ratio, while avoiding PMT saturation. PMT gain calibration is performed with a pulsed LED in order to correct for results obtained at different PMT voltages. For convenience, PMT waveforms are acquired with a sampling time of approximately 3.5 ns. Prior to data analysis, a background discrimination algorithm rejects events based on waveform duration, time offset, and shape, as well as on baseline cleanliness.

Figure 8(a) depicts a typical waveform. The amplitude growth over time results from the increasing solid angle subtended by the PMT window as the electron cloud drifts toward the anode. However, when the reduced electric field is below the EL threshold, the PMT waveform reveals features that would otherwise go unnoticed, as shown in Fig. 8(b). The first short peak corresponds to the primary-scintillation signal (S1) from the alpha particle interaction, while the last, longer peak results from the secondary scintillation (S2) produced when the ionization electrons are close to the anode strips, where the nonuniform electric field is above the EL threshold. According to simulations, the electric field at 30 μm, 1 μm, and 50 nm away from the anode strips can be, respectively, 2, 10, and 50 times higher than the average electric field. In addition, various smaller and shorter peaks can be observed between the two major ones, which is a phenomenon that can be unambiguously assigned to single-photon emission during the drift of the ionization electrons.

Our interpretation of the origin of the "start" and "end" features of the waveforms shown in Fig. 8 can be confirmed by comparison with the expected electron drift velocity in pure xenon. This is obtained, for each run, from both the distribution of waveform duration and the mean range of the alpha particles along the electric field direction (from SRIM). The start of event is given by the instant the waveform amplitude rises by 5% of its maximum height, while the end of event is defined as the instant the center of the electron cloud reaches the anode. For low-field waveforms [Fig. 8(b)], that instant corresponds to the centroid of the diffusion-dominated S2 peak, while for high electric fields [Fig. 8(a)], it corresponds to the instant the amplitude falls to 65% of the waveform maximum. This last value is estimated by simulating the drift diffusion of the electron cloud, considering the detector geometry and the PMT response function. Nonetheless, there is a transition between the two distinct waveform shapes when the electric field reaches values close to the EL threshold. In this case, the end of event is linearly interpolated between the waveform maximum and the 65% threshold. The electron drift velocity obtained with this procedure is depicted in Fig. 9 for several E/p values together with the simulated curve from PYBOLTZ. The agreement between experimental and simulated data is acceptable, and the
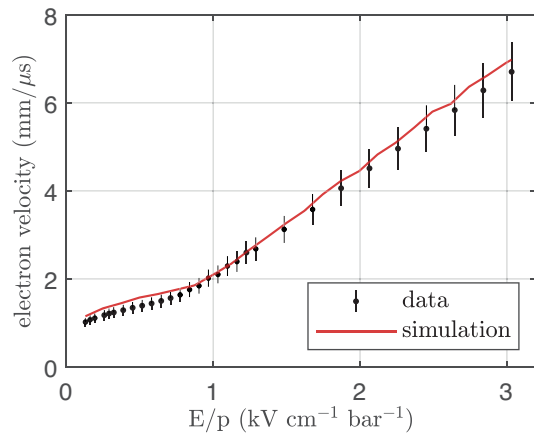
FIG. 9. Electron drift velocity determined from the driftless GPSC waveforms as a function of pressure-reduced electric field E/p, compared with the simulated curve obtained from PYBOLTZ.

observed deviation is included as a contribution to the overall systematic uncertainty of the scintillation yield per unit path length.

Because of the angular distribution of the alpha particles and the presence of the entrance window and degrading foil, a selection cut on the primary ionization has to be applied. Figure 10(a) shows the typical energy spectrum for alpha particles obtained from the histogram of the waveform integrals. The lack of events at low energies results from the oscilloscope trigger threshold. A ^{55}Fe radioactive source is used to calibrate the detector energy for a given E/p value, chosen as 2.9 kV cm^{-1} bar^{-1}. In this way, a peak energy of 1.9 MeV is measured for alpha particles, which is in good agreement with the SRIM simulated value of 1.7 MeV. Since the shape of the energy spectrum is found to not depend significantly on E/p, the peak of the distribution is used to calibrate the remaining datasets acquired for each E/p value. A kernel density estimation assuming a normal kernel function and a bandwidth of about 170 keV are used to smooth the experimental energy distribution, hence reducing fluctuations of the distribution peak position. The recombination of electron-ion pairs produced by the alpha particle interaction is expected to be negligible for the relatively high E/p values studied in this work [80]. Between 399 and 132 V cm^{-1} bar^{-1}, we find a variation of only $(0.3 \pm 2)\%$ in the primary-scintillation yield, which is anticorrelated with the number of ionization electrons. Moreover, for E/p values down to 40 V cm^{-1} bar^{-1}, the primary-scintillation yield is observed to vary less than 5%.

To reduce the influence of the oscilloscope trigger threshold, a 1.6-MeV energy cut is applied to the data. The error introduced by this cut is included in the uncertainty of the measured yield values. Finally, in order to determine the scintillation yield, it is desirable to select a waveform region that is (i) sufficiently delayed with respect to S1 to exclude the Xe deexcitation tail of the triplet state

as well as any PMT after pulsing and (ii) sufficiently ahead of the diffusion-dominated anode signal. Hence, a short region of interest (ROI) is defined midway between the instant the event starts and the instant it ends, accounting for the photons emitted while the electron cloud is positioned between 0.9 and 1.3 cm away from the anode. An important side benefit of this procedure is the simplification of the geometrical corrections needed for comparison with simulation. Afterward, the average of the waveform integrals performed in the 4-mm ROI (in blue in Fig. 8) is computed, subtracting the integrated baseline prior to the event (in red in Fig. 8). The yield estimated in this way can be calibrated to an absolute number of photoelectrons per unit path length, after considering the integral signal produced by single photoelectrons, as determined beforehand for photons emitted by a blue LED supplied with direct current.

For low electric fields, the aforementioned technique loses precision, as the NBrS emission is at the level of the baseline fluctuations, requiring large statistics. However, since the NBrS signal consists mostly of individual photon peaks [see Fig. 8(b)], single-photon counting techniques may be applied. For pressure-reduced electric fields below 0.4 kV cm^{-1} bar^{-1}, photoelectron peaks that have a typical FWHM duration of 6 ns are already sparse enough to be counted. For instance, a density of 42 and 1.3 photoelectrons per microsecond is estimated for 399 and 132 V cm^{-1} bar^{-1}, respectively. However, due to the low PMT gain, most of the photoelectron peaks are masked by high-frequency noise preventing us from computing the total number of photoelectrons from the number of peaks. For this reason, we rely on peak areas with the additional advantage of accounting for double-photoelectron events as well. To reduce the effect of low-frequency baseline fluctuations, the ROI is processed in a software high-pass filter with a time constant of 20 ns. Afterward, every peak found in this region and above a given threshold is integrated. Figure 10(b) shows an example of the distribution of integrals for these peaks and for an E/p value of 300 V cm^{-1} bar^{-1}. Finally, a suitable fit function is used to estimate the total number of detected photons that is subsequently normalized to the number of events. This function is shown in Fig. 10(b) and consists of a sum of five Gaussian functions where the first one accounts for the high-frequency noise of the signal with area, centroid, and sigma being left as free parameters, while the subsequent account for single-, double-, triple-, and quadruple-photoelectron detection. Their centroids follow the scaling $1pe$, $2pe$, $3pe$, and $4pe$, respectively, where pe is the centroid of the single-photoelectron Gaussian with standard deviations σ, $\sqrt{1}\sigma$, $\sqrt{2}\sigma$, $\sqrt{3}\sigma$, and $\sqrt{4}\sigma$, respectively, the areas being related through Poisson statistics. The rate parameter of the Poisson distribution, the centroid, and the standard deviation of the single-photoelectron Gaussian are left as free parameters. Results from both photon counting and the integral method are presented in the next section.
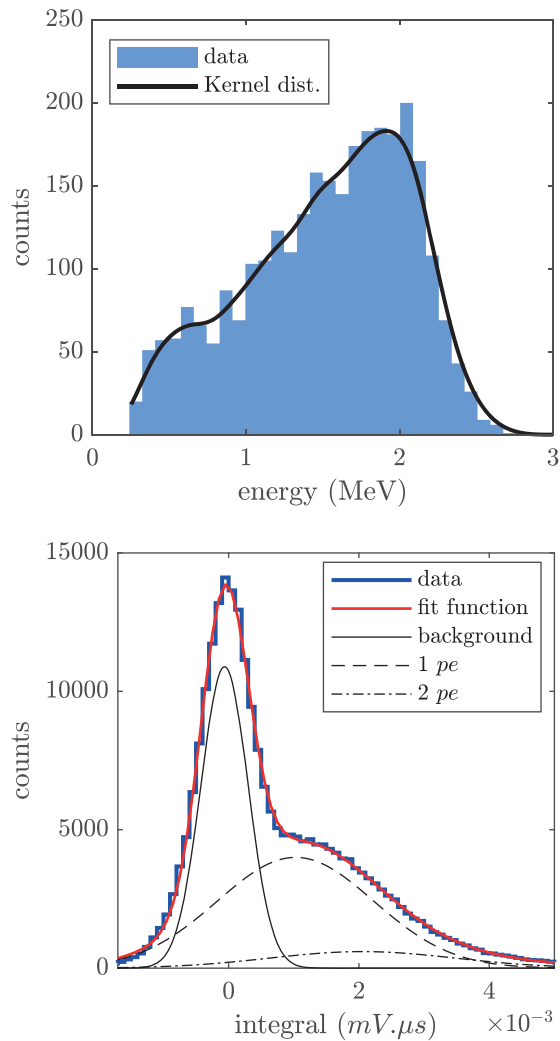
FIG. 10.   (a) Typical energy spectrum of alpha particles in the GPSC detector taken for an E/p value of 1.5 kV cm^{-1} bar^{-1}, fitted to a kernel distribution in order to estimate the peak energy. (b) Distribution of the integral of photoelectron pulses, obtained for a low E/p value (300 V cm^{-1} bar^{-1}), in the waveform ROI. It is fitted to a sum of Gaussian distributions, accounting for the background, single-, double-, triple-, and quadruple-photoelectron detection, the latter two not being visible in the graph.

Electric field maps of the GPSC are obtained using a finite element method solver [81]. The electric field is found to vary by 15% along the 2.45-cm absorption region and by 5% in the 4-mm-long × 8.5-mm-wide ROI, with the latter dimension defined by the requirement that 95% of the transversely diffused electrons are contained within it. Henceforth, reported E/p values correspond to the average reduced electric field in the ROI.

IV. EXPERIMENTAL RESULTS AND DISCUSSION

The xenon secondary scintillation yield as measured over 5 orders of magnitude in E/p is shown in Fig. 11 (a table with the numerical data can be found as the Appendix).

The yield is normalized to the gas pressure, path length, and number of ionization electrons. The latter is obtained from the average energy deposited by alpha particles in the gas after performing the aforementioned 1.6-MeV cut and assuming a W_I value of 21.9 eV, i.e., the mean energy required to produce an electron-ion pair (see Ref. [82] and references therein). Two datasets are shown, one of them obtained using the waveform averages (blue markers) and the other one, for low E/p values, obtained by photon counting (red markers) as discussed in Sec. III B. For E/p values below 400 V cm^{-1} bar^{-1}, the scintillation in the ROI is sufficiently low to enable the use of the more precise photon counting method. When E/p is around 350 V cm^{-1} bar^{-1}, our standard analysis based on the waveform average is still precise, allowing for a direct comparison between both methods. The good agreement observed in this region shows the accuracy of the photon counting method, which becomes more reliable for lower electric fields. The error bars represent the 68% confidence level regions comprising both systematic and statistical uncertainties associated with the analysis methodology and instrumental limitations; a list of the different uncertainty sources can be found in the Appendix. An inflection point can be observed in the experimental data at E/p values below the EL threshold, suggesting the existence of a different emission mechanism in that region. This emission, despite being weak, remains measurable at around 2 orders of magnitude below its yield at the intercept point of the two contributions, with sensitivity ultimately limited by the QE of the PMT.

A. Assessment of the subthreshold emission and its nature

The time distribution of NBrS photons should obey Poisson statistics; otherwise, a correlation in photoelectron events may suggest a different mechanism for the observed subthreshold signal, e.g., PMT after pulsing or long-lived excited states from impurities produced in correlation with the primary-scintillation signal. At very low electric fields, photoelectron peaks are sparse enough to be binned in time. Therefore, the time between consecutive photoelectrons can be computed considering the same narrow waveform region used for NBrS yield measurements. For this measurement, the peak detection threshold is set to a high value (350 μV, 3σ above the electronic noise) to avoid triggering into noise spikes, though with a 30% loss in photoelectron events. Figure 12 depicts the distribution of the time between photoelectrons obtained from 1500 waveforms for three different electric field values. As expected, the time distribution of photoelectrons follows an exponential function, also shown in the figure. The small deviation between data and fit function observed for short durations is attributed to the difficulty in distinguishing neighboring photoelectron peaks.
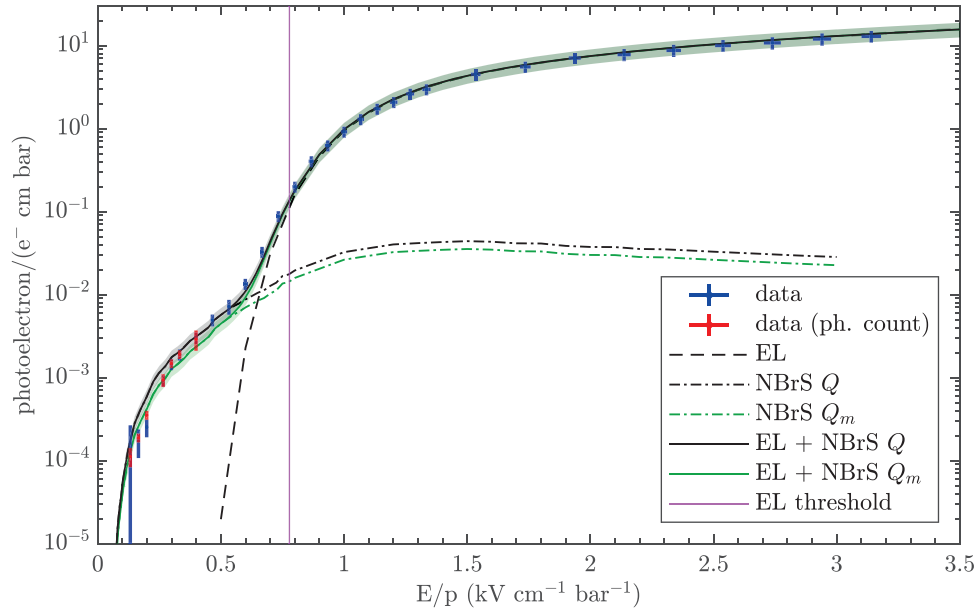
FIG. 11. Number of detected photoelectrons obtained with the driftless GPSC as a function of the reduced electric field, the value being normalized according to the gas pressure, drift path, and number of primary ionization electrons. At low electric fields, the experimental results obtained with the photon counting method are also shown (points in red). Error bars present the 68% confidence levels of the experimental data. As defined at the end of Sec. III B, the EL threshold is obtained from a linear fit to the EL yield data for E/p values above 1 kV cm^{-1} bar^{-1}, where the yield dependence on E/P is approximately linear. Simulated curves are superimposed to the data, the NBrS yield being obtained by assuming proportionality with either Q or Q_m. Colored bands present the systematic error associated to the simulation curves, dominated by the 20% uncertainty estimated for the detection efficiency.

In order to better disentangle the different contributions to the measured scintillation signal, we proceeded as follows: The emission at high E/p values (assumed to be excimer-based, hence EL emission) is simulated with the microscopic package introduced in Ref. [42], while the emission at low E/p values (assumed to be NBrS) is
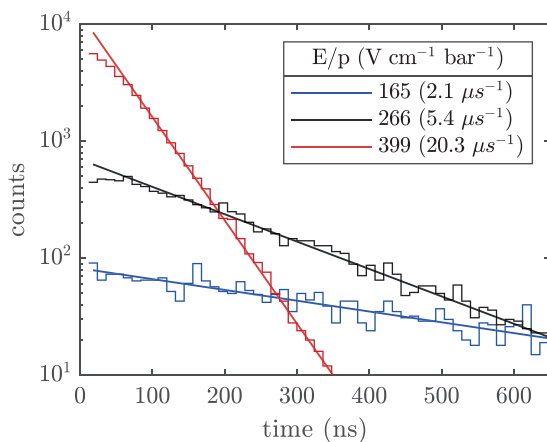

FIG. 12. Distribution of time elapsed between photoelectron events in the NBrS region obtained from 1500 waveforms for three different electric field values. An exponential function is fitted to each dataset; the photoelectron rates obtained from the fits are shown in the legend.

determined using the new features of the recently developed PYTHON-version of the Magboltz code Pyboltz [60], allowing for an implementation of the theoretical framework described in Sec. II. The final calculation of the number of photoelectrons requires taking into account the wavelength-dependent PMT quantum efficiency QE(λ) and geometrical efficiency GE(λ), shown in Fig. 2. The QE is obtained from the manufacturer and GE from a Geant4 simulation [83] [Fig. 13(top)]. As a result of the dependence of the NBrS emission spectrum on E/p, the detection efficiency ($\mathcal{D}$) becomes field dependent. Its value, averaged over the range of 120–1000 nm ($\mathcal{D} = \langle QE \times GE \rangle_\lambda$), is shown in Fig. 13(bottom). The systematic uncertainty in the simulated photoelectron yield in Fig. 11 is expected to be dominated by the estimated 20% uncertainty in the detection efficiency for both EL and NBrS components and for all E/p values.

Even though the probability of double-photoelectron emission (DPE) from the PMT photocathode is negligible in the visible region, it may reach 20% for VUV photons [84]. Since we measure the total number of photoelectrons in both photon counting and waveform integral method, our experimental results contain the wavelength-dependent DPE effect. However, this issue does not affect the comparison between experimental data and simulation, as the latter is computed using the PMT QE curve provided by the manufacturer, which also includes this effect.
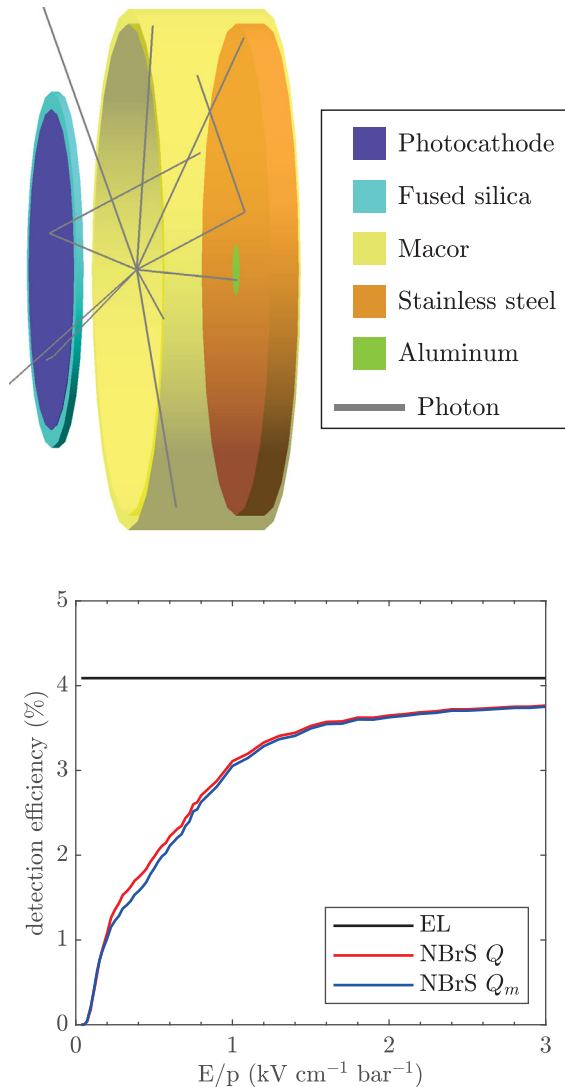
FIG. 13. Top: geometry used in Geant4 for the calculation of the light collection efficiency of the driftless GPSC, including the most relevant detector materials. The transparency of the anode grid ($\mathcal{T} = 81\%$) is included as a multiplication factor over the simulated value. Bottom: the overall detection efficiency averaged over the 120–1000 nm range ($\mathcal{D} = \langle QE \times GE \rangle_\lambda$) is shown as a function of reduced electric field E/p, considering both EL and NBrS spectra. A dependence with either Q or Q_m is assumed in Eq. (10). A 20% uncertainty is estimated for $\mathcal{D}$, being dominated by the uncertainty in GE and obtained by varying the optical parameters in the simulation (Macor, stainless steel, and aluminum reflectivity).

Ultimately, comparison of data with simulation yields $\mathcal{X}^2/\text{d.o.f.} = 2.72$ for Q_m and 13.59 for Q in the range of E/p values up to 500 V cm^{-1} bar^{-1}. This agreement makes a compelling case for NBrS as the source of the observed subthreshold emission with a clear preference for Q_m in the present conditions. Despite the good visual and statistical agreement, the relatively high $\mathcal{X}^2/\text{d.o.f.}$ value motivates further work on both theoretical and experimental fronts, in

the latter case, for instance, through measurements at different wavelengths.

From the theoretical point of view, it is relevant to note that the proportionality of the NBrS yield with Q is derived in Ref. [56] starting from Fermi's golden rule together with the inclusion of the waveforms and orbitals involved as partial-wave solutions of the radial Schrödinger equation. Two key approximations are introduced: (i) The target is a single-atom species; (ii) only the first two terms of the partial-wave expansion (s, p) are involved in the interaction. Strictly speaking, the latter approximation begins to lose accuracy for electron energies around and above the Ramsauer minimum ($\varepsilon = 0.75$ eV in Xe), as shown for instance in Ref. [85], a fact that might explain part of the observed discrepancy between data and simulation; the average electron energy for 100 V cm^{-1} bar^{-1} is already slightly above 1 eV and exceeds 3 eV at 1 kV cm^{-1} bar^{-1}. On the other hand, the proportionality of the NBrS yield with Q_m is obtained by treating the interaction with the Lippmann-Schwinger equation, taking the low photon-energy limit ($h\nu/\varepsilon < 1$; see Ref. [58]). Interestingly, and contrary to Ref. [56], this derivation is thus valid for all wave orders and independent from the electron energy (electric field), which may explain the better overall agreement between data and simulation. Despite the ratio between the average photon and electron energies being relatively high in the region covered by the PMT ($\langle h\nu \rangle / \langle \varepsilon \rangle = 0.8$–0.9 in the range of 100–600 Vcm^{-1} bar^{-1} according to simulation), the "low photon-energy limit" presents a reasonable first-order approximation, given that the subdominant terms in Ref. [58] are strongly suppressed as $(\nu/\varepsilon)^2 \times (\nu/k)^3$.

Before more refined theoretical calculations become available, a purely model-independent way to assess the radiative nature of the emission is desirable. This can be accomplished through the addition of a controlled trace amount of molecular additive as an "impurity," in this case chosen to be C_2H_6 at a molar concentration of 0.12%. As in previous work [33,54], the concentration is monitored during data taking with a residual gas analyzer together with a sampling system in order to eliminate effects related to getter absorption of the additive. The two experimental methods, integral and photon counting, are statistically combined and are shown in Fig. 14(top). The shift of the features in the Xe-C_2H_6 data series toward higher E/p values than in pure xenon is due to electron cooling, enhanced through inelastic transfers to vibrational and rotational states of the molecular additive [33,43,54]. In the presence of these transfers, the electric field needs to be higher to compensate for energy lost by electrons to the molecules, to achieve a similar equilibrium electron energy distribution. Notably (although irrelevant for the following argument), simulation reproduces this effect accurately. According to earlier studies of EL in the presence of molecular additives [86], the electron cooling effect can be compensated by applying a suitable shift to the reduced
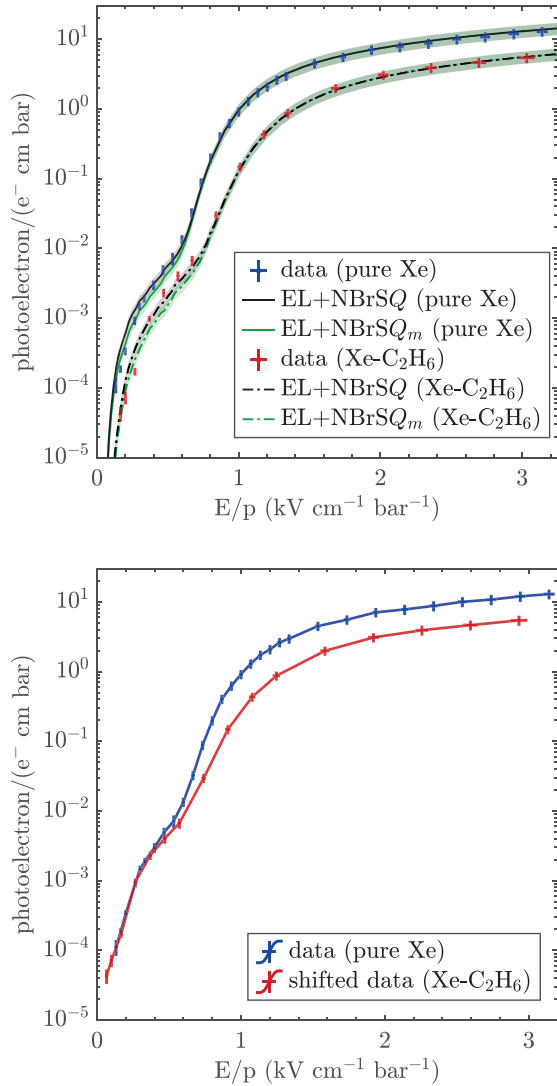
FIG. 14. Top: the number of photoelectrons (68% confidence level depicted as error bars) obtained experimentally with pure Xe and a Xe-C_2H_6 admixture (with a 0.12% C_2H_6 molar concentration), together with the respective simulated curves (systematic error depicted as colored bands). The experimental results provided by the two analysis methods for low electric fields are statistically combined. Bottom: the Xe-C_2H_6 curve is shifted to the left by 100 V cm^{-1} bar^{-1}, illustrating the different nature of the low-E/p emission, since it is not quenched, unlike the EL (excimer-based) contribution.

electric field, which in this case is determined to be 100 V cm^{-1} bar^{-1} corresponding to the increment in the EL threshold (as defined in Sec. III A) and implemented in Fig. 14(bottom). After accounting for electron cooling in this approximate way, we find that the impact of the additive on the scintillation occurring at low E/p is negligible, and the NBrS emission can be fully recovered, in contrast to the case for high E/p values, where the EL suffers permanent losses due to quenching of the excited xenon triplet states by molecular additives. The impact of
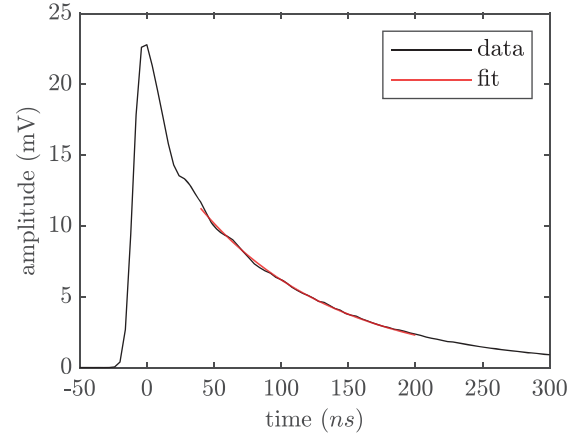

FIG. 15. Average S1 waveform and exponential fit in the triplet-dominated region for a reduced electric field E/p, of 132 V cm^{-1} bar^{-1}. The decay time obtained from the fit is $\tau_3 = 100.7 \pm 1.2$ ns.

C_2H_6 on NBrS and EL emission is also simulated, as shown in Fig. 14(top). Concerning the EL contribution, the quenching probability P_Q is left as a free parameter with a best description of data found for a scintillation probability of $P_{scin} = 1 - P_Q = 55\%$, a value that acts as a global factor multiplying the EL contribution for all fields. An independent estimate considering the simple model in Eq. (10) of Ref. [43] yields $P_{scin} = 37\%$ when the quenching rate of the first excited state of Xe in the presence of C_2H_6 is introduced, as measured by Velazco, Kolts, and Setser [87].

Unintentional gas contamination by impurities from system outgassing might still be invoked to explain the observed subthreshold scintillation. Besides the accurate description of the EL yield in pure xenon, additional evidence of the minimal impact of impurities in the GPSC can be found by consideration of the primary-scintillation signals. At low electric fields, below 400 V cm^{-1} bar^{-1}, they become distinguishable from both EL and NBrS emission, and the same method used to compute the secondary-scintillation yield from waveform averages can be employed. For the studied E/p range, the mean energy required to produce a primary-scintillation photon is estimated to be $W_{sc} = 53.5 \pm 3.9 (\text{stat}) \pm 13.5 (\text{sys})$ eV, which is in good agreement with the values reported in the literature [88,89]. Usually, the time constant of the triplet state of xenon can be determined with a precision that makes it more sensitive to impurities than the yields themselves. In our case, a value of $\tau_3 = 100.7 \pm 1.2$ ns is obtained (Fig. 15), to be compared with an average reference value of $\tau_3 = 100.9 \pm 0.7$ ns [90]. An upper limit for the gas contamination in our system can be estimated from the experimental triplet lifetime using, for instance, Eq. (1) in Ref. [43] together with the two-body quenching rates for excited Xe atoms reported for N_2, CO_2, O_2, and CH_4 in Ref. [87] and for H_2O in Ref. [91].

In this way, an upper limit of 7 ppm can be assessed for H_2O, O_2, CO_2, and CH_4 concentrations at 95% confidence level, and, in general, lower values can be derived for heavier molecules based on the same references. Lower quenching rates for N_2 lead to an upper limit of 135 ppm. However, even percent levels of N_2 in Xe are known not to cause measurable reemission both in the UV and in the visible region, as shown in Ref. [92]. Alternative explanations for the observed phenomenon other than NBrS need to be compatible with these stringent purity limits.

B. Impact of NBrS on present xenon TPCs and possible applications

From Fig. 11, one can see that, in our system, the NBrS contribution to the secondary scintillation is less than 1% for EL-field values above 1.5 kV cm^{-1} bar^{-1}. A similar value can be inferred from the results presented in Fig. 6 for the NEXT-White TPC. This yield is insufficient to modify the calorimetric response of the detector in a perceptible manner. In spite of its negligible contribution to secondary scintillation in the regular physics runs of NEXT-White, Fig. 11 shows that NBrS represents up to 30% of the signal for α runs, since those are typically obtained at pressure-reduced electric fields in the scintillation region around $E/p = 0.62$ kV cm^{-1} bar^{-1} in order to avoid PMT saturation. Furthermore, energy peaks from α particles can be reconstructed down to fields as low as 200–500 V cm^{-1} bar^{-1} in the absence of excimer (VUV) emission. This invites the possibility of combining NBrS and Geant4 simulations to benchmark the optical response of the NEXT-White TPC for α runs in scintillation conditions under which wavelength-shifting effects play no role. In this way, comparison with x-ray and γ-ray runs at higher EL fields could provide access to the absolute wavelength-shifting efficiency (W_{LSE}) and uniformity of the TPB coating used in the anode plane of the EL region, which is a critical parameter for calorimetry.

Clearly, for typical drift fields around 40 V cm^{-1} bar^{-1}, PMTs are largely blind to NBrS due to their lack of sensitivity above 650 nm. The SiPM plane behind the EL region, despite being sensitive in this range, lacks the necessary coverage. The cathode voltage, however, has an important side effect in NEXT-White, affecting the "buffer region" between the cathode and the (grounded) PMT plane that is used for grading the field and avoiding sparking and PMT instabilities due to transient fields. The electric field in that region, which is chosen to be lower than the EL threshold, can still reach several hundreds of V cm^{-1} bar^{-1} during operation, producing strong NBrS scintillation in a region particularly close to the PMT plane. These signals, largely arising from cathode plating by Rn progeny, are observed in the NEXT-White TPC and display durations corresponding to the electron drift time in this region. In light of this work, they can now be interpreted as S1 signals with an NBrS tail. Usually, this

type of signal as well as field emission at the cathode creates optical background that interfere with the ability to distinguish and/or to measure precisely the low-photon (S1) signals produced in the drift region (e.g., for ^{83m}Kr events distant from the cathode). Our observations contradict the conventional understanding that the only consideration determining the upper limit for buffer electric field strengths is that the buffer electric field be below the EL threshold. This conclusion can be extended to the buffer regions in double-phase TPCs, as shown below. Our results demonstrate that one has to weigh the electric field intensity and, thus, the buffer region thickness, with the tolerable amount of NBrS for the scintillation background goals to be aimed, especially when lower-amplitude signals, e.g., lower WIMP mass regions, are to be targeted.

The performance of alternative photosensors, in particular SiPMs, is currently being investigated for operation in LXe (e.g., Ref. [93]), and they are considered as an alternative to PMTs in future xenon-based detectors such as nEXO [94] and DARWIN [4], as well as argon-based experiments such as DarkSide-20k [95]. These photosensors are currently in use in NEXT for the (sparsely instrumented) tracking plane and considered as a possible PMT replacement for future upgrades of the (densely instrumented) energy plane. These photosensors have different spectral responses to the PMTs used in this work, and, thus, light yield results that are not convolved with a PMT spectral response are of interest. Figure 16 presents the simulated, data-validated scintillation yield (at the production point) for xenon gas, integrated over the 120–650 nm and 120–1000 nm regions. The choice of SiPMs is largely driven by radio purity considerations, at the expense of increased dark count rate. However, their extended sensitivity up to nearly 1000 nm implies that, for drift fields as low as 30–50 V cm^{-1} bar^{-1} in xenon gas, NBrS yield values per e^- cm^{-1} bar^{-1} would already be at the levels reported in this work. Hence, it can be expected that, besides background scintillation from the buffer region, any interaction in the TPC will produce a significant amount of light during electron drift from cathode to anode.

To estimate the relative yield of NBrS to primary scintillation, we recall that every primary photon is produced in association with ionization electrons in a ratio of $W_I/W_{sc} = 0.3$ primary photons per primary electron. $W_I = 21.9 \pm 0.2$ eV/e^- and $W_{sc} = 71.6 \pm 5$ eV photon^{-1} are obtained from the weighted average of the values presented in Ref. [82] and references therein for W_I and in Refs. [26,28,96] for W_{sc}, for both electron and gamma interactions. For events originating at the cathode, the spurious scintillation from NBrS emitted during electron transit will likely exceed that from primary scintillation, since already in NEXT-White the ratio is $Y_{NBrS}/Y_{S1} = 10.23$, as shown in Table I. The average effect per event in NEXT-White can be estimated
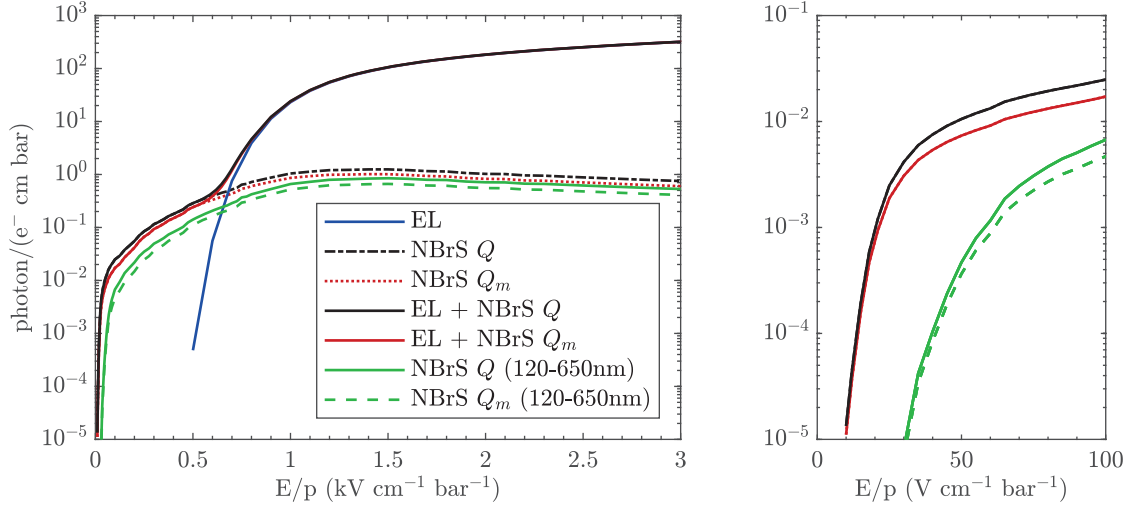
FIG. 16.   Simulated secondary-scintillation yield in the range of 120–1000 nm as a function of E/p. A dependence with either Q or Q_m is assumed in Eq. (7). The individual contributions from EL and NBrS are shown ($T = 300$ K). A detail of the 0–100 $V\,cm^{-1}\,bar^{-1}$ region is shown on the right side. For comparison, the simulated NBrS yield in the 120–650 nm range is also plotted.

by evaluating Y_{NBrS} at the center of the drift region, leading to a ratio of 5.1.

We may also consider the impact of the NBrS signal on the measurement of S1 signals, which unlike the NBrS signal are tightly bunched within an order-of-100-ns time window around the interaction time. Even considering the sparse nature of NBrS, about 88 $ph\,MeV^{-1}$ are expected in a typical S1 window around 300 ns, to be compared with 590 photons released for a typical S1 signal from ^{83m}Kr. The above NBrS yields increase by a factor of 4 at pressure-reduced drift fields of 100 $V\,cm^{-1}\,bar^{-1}$ (design goal). Hence, and given its sparse and continuous nature and

much more favorable detection characteristics than excimer emission, NBrS almost certainly dominates the luminous background to S1 reconstruction for SiPM-based HPXe-TPCs. For drift fields below 10 $V\,cm^{-1}\,bar^{-1}$, the electron energy distribution becomes thermal and, therefore, shifts the wavelength cutoff up to around 4000 nm, though operation in these conditions is impractical due to enhanced electron attachment and diffusion.

The results obtained from our simulations are more than one order of magnitude lower than the single absolute NBrS yield value previously presented in Ref. [45], for 100 $V\,cm^{-1}\,bar^{-1}$, and obtained directly from Eq. [1,45],

TABLE I.   Compilation of simulated neutral bremsstrahlung yields (120–1000 nm) obtained for the technical specifications of various noble element TPCs [53,94,97]. The skin or veto field and size in LZ refers to the average in the cathode region. The ratio of neutral bremsstrahlung to primary-scintillation yield ($Y_{\mathrm{NBrS}}/Y_{\mathrm{S1}}$) corresponds to full electron transit across the considered region, using W_I and W_{sc} given in the text. For the liquid phase, a constant drift velocity of $v_d = 2.8$ mm μs^{-1} in the region of 3–10 $kV\,cm^{-1}$ [98] is assumed, while $v_d = 1$–1.5 mm μs^{-1} is assumed for xenon gas, as obtained during the present measurements. The calculations assume proportionality with Q_m in all cases.

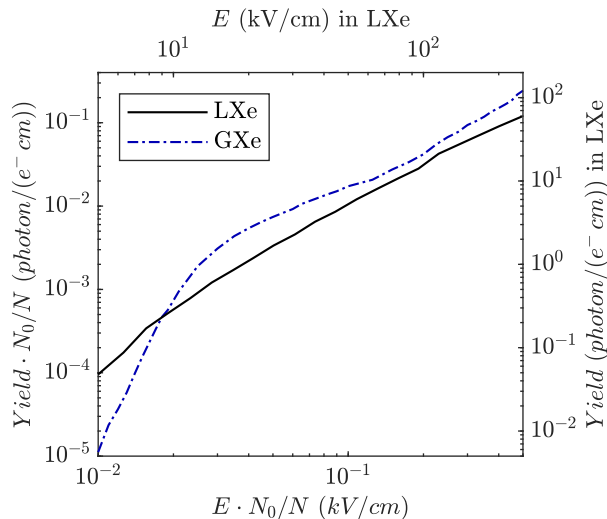|		NEXT-White			
Region	E/p ($kV\,cm^{-1}\,bar^{-1}$)	Size (cm)	ph/e^{-1}	$Y_{\mathrm{NBrS}}/Y_{\mathrm{S1}}$	ph/MeV (300 ns)
Drift	0.044	53	3.08	10.27	88
Buffer	0.26	12.9	7.87	26.23	1388
		LZ			
Region	E ($kV\,cm^{-1}$)	Size (cm)	ph/e^{-1}	$Y_{\mathrm{NBrS}}/Y_{\mathrm{S1}}$	ph/MeV (300 ns)
Drift	0.3–0.6	145.6	$\cdots$	$\cdots$	$\cdots$
Reverse field	3–6	13.75	0.17–1.13	0.15–1.00	74–490
Skin field	5–10	8	0.41–2.56	0.36–2.27	270–1700
		n-EXO			
Region	E ($kV\,cm^{-1}$)	Size (cm)	ph/e^{-1}	$Y_{\mathrm{NBrS}}/Y_{\mathrm{S1}}$	ph/MeV (300 ns)
Drift	0.4	125	$\cdots$	$\cdots$	$\cdots$
Buffer	10	5	1.60	1.41	1700

FIG. 17. Calculations of the density-reduced neutral bremsstrahlung yields in the range of 120–1000 nm, for xenon gas (blue) and liquid (black) as a function of density-reduced electric field E/N. Proportionality with Q_m is assumed in Eq. (7). Magnitudes appear normalized to the number of molecules per unit volume at normal gas conditions (N_0). For easier reading, the other two axes show the absolute yields and electric fields corresponding to the liquid phase. Although at low reduced fields N scaling is not a good assumption, for fields above $10 \, \mathrm{kV \, cm^{-1}}$ in liquid xenon it becomes accurate within a factor of 2.

which we believe does not correctly describe NBrS. No direct comparison between experimental results and theoretical values is attempted, and when evaluating Eq. [1] the authors of Ref. [45] assume an electron drift velocity of $1 \, \mathrm{mm \, \mu s^{-1}}$, an average instantaneous electron velocity of $10^8 \, \mathrm{cm \, s^{-1}}$ ($\varepsilon = 3$ eV), and an elastic cross section of $10^{15} \, \mathrm{cm^2}$. However, at $100 \, \mathrm{V \, cm^{-1} \, bar^{-1}}$, the typical electron energies are well within the deep Ramsauer minimum, where the cross sections vary up to 2 orders of magnitude, and NBrS yield calculations cannot be reproduced through that simple equation.

Finally, the discussion on the impact of NBrS in xenon TPCs can be extended to the liquid phase. We use the first-principles cross sections recently obtained in Ref. [98] and apply the same theoretical framework developed for gaseous xenon in the present work. Results from this calculation are shown in Fig. 17 with the axes showing density-reduced units (E/N, Y/N), for direct comparison. For convenience, the magnitudes refer to the number of molecules per unit volume at normal conditions ($T = 20\,°C$, $P = 1$ atm), $N_0 = 2.504 \times 10^{25} \, \mathrm{cm^{-3}}$ (the density ratio between xenon gas at normal conditions and liquid xenon is about a factor of 500). The equivalences in yields per electron-cm and electric field in $\mathrm{kV \, cm^{-1}}$ for the case of liquid are given on the right and top axes,

respectively. Since single- and double-phase TPCs operate at considerably lower density-reduced drift fields (E/N) than gaseous TPCs, NBrS produced in these conditions has a much smaller impact. This can be seen clearly in both Fig. 17 and Table I. While NBrS yields in the drift region of modern liquid xenon TPCs are likely to be very small, it is anticipated that buffer and skin (veto) regions produce NBrS scintillation in liquid xenon at similar levels to those in gas detectors (Table I) when the total number of photons per MeV of energy deposit is integrated. In this case, we take $W_I = 15.6$ eV and $W_{sc} = 13.8$ eV from Ref. [99]. While the impact of this scintillation on S1 reconstruction depends on the achievable detector background and details of the reconstruction procedures, it seems clear that NBrS will be a very apparent feature in upcoming LXe-based TPCs like LZ or nEXO. As long as the veto and active regions are optically decoupled, NBrS emission in the veto will not affect the TPC response.

An attractive possibility arises from the calculation in Fig. 17: the operation of a scintillation region in LXe at an electric field of $100 \, \mathrm{kV \, cm^{-1}}$, a factor of 4 below the breakdown field reported in Ref. [100]. Calculations for liquid anticipate a NBrS scintillation yield of 17 ph/e^- cm^{-1}, while a direct application of density scaling from gas leads to 50 ph/e^- cm^{-1}. Given the unusual characteristics and faint nature of this phenomenon, it is conceivable that it might have gone unnoticed in previous experiments in liquid, or else misinterpreted, as recently referenced in Ref. [101]. Moreover, a recent review of the historical efforts toward achieving electroluminescence in liquid Xe [102] estimates the achievable EL yields to be around 20 ph/e^-, for 10-μm wires, thus similar to the values expected from NBrS in a 1-cm-thick uniform field region capable of sustaining a 100-kV voltage drop. Such electric field intensities have been successfully applied in LAr [103] and, hence, are quite feasible in LXe. Hole structures can be envisaged as an alternative to parallel mesh, uniform field geometry. Although such high-voltage values are clearly challenging for most amplification structures, operation of very thick (0.5-cm) PMMA structures machined following micropattern gas detector (MPGD) fabrication techniques is demonstrated that can hold up to 27 kV/cm in Xe at 10 bar [41], i.e., at 50 times less density than LXe. This means that, on the one hand, obtaining yields of around 200 ph/e^- as those needed to reconstruct low-energy events (for low-mass WIMP searches, for instance [102]) would require MPGD structures to be tailored to enhance light-collection efficiency [104], as well as further thickened in order to increase the yields. On the other hand, concerning detection of high-energy events in experiments resorting to calorimetry (such as for $\beta\beta0\nu$ searches [94]), a direct use of the conventional formula for EL (e.g., Ref. [41]) leads to an estimate of the instrumental contribution to the energy resolution of

$$\text{res} = 2.35\sqrt{Q_{\text{EL}} + \frac{1}{N_{pe}}\left[1 + \left(\frac{\sigma_G}{G}\right)^2\right]}\sqrt{\frac{W_I}{\varepsilon}} \quad (10)$$

with Q_{EL} being the intrinsic fluctuations of the EL process, much smaller than 1, N_{pe} the number of photons detected, and σ_G/G the relative spread of the single-photon distribution of the photodetection sensor. Even in the unfavorable case where $\sigma_G/G = 1$ (SiPMs can perform a factor of about 10× better), a very modest value of $N_{pe} = 1$ would suffice to set an instrumental resolution at the 1%(FWHM) level for the $Q_{\beta\beta}$ value of ^{136}Xe ($\varepsilon = 2.45$ MeV), at least a factor ×2 better than the best values achieved so far in LXe [76,94]. Based on our calculations, even existing structures without further optimization [41] would likely accomplish this task.

Clearly, new calculations and fundamental measurements of NBrS are needed, in controlled conditions as well as in ongoing gas and liquid-phase experiments. Of particular interest are the spectral content, the accurate calculation of the matrix element, and a proper accounting of medium effects in liquid transport. From a technological standpoint, the energy resolution, yields, and stability achievable using NBrS scintillation in thick-gap structures instead of wires remain to be seen. Despite the difficulties ahead, it would seem that the reward of such a research program might be very high.

V. CONCLUSIONS

In this paper, we present the first unambiguous identification of NBrS luminescence in xenon, supported by a predictive theoretical model of this light emission process. We present compelling evidence of photons being emitted by low-energy ionization electrons in the induced dipole field of xenon atoms at electric field strengths of interest for TPCs used in rare event searches. We have shown its presence in the NEXT-White TPC, currently the largest optical HPXe-TPC in operation; and we have performed detailed measurements in a dedicated setup and implemented a robust theoretical model for NBrS, which describes the data very well.

NBrS emission is intrinsically broadband and, as confirmed by our measurements, immune to quenching mechanisms, unlike conventional excimer-based electroluminescence emission. Since it does not create additional electrons nor ions, NBrS is expected to be free from ion feedback or ageing issues. This mechanism produces scintillation levels that are detectable with standard sensors over a range of density-reduced electric fields, extending from those employed for secondary scintillation (e.g., EL) to typical drift fields.

For nominal EL-field values above 1 kV cm^{-1} bar^{-1} in the gas phase, the NBrS contribution to the secondary scintillation is less than 1%, insufficient to modify the calorimetric response of xenon TPCs in a perceptible manner. Similarly, for typical drift fields below 50 V cm^{-1} bar^{-1}, the NBrS emission falls below the sensitivity range of conventional PMTs, as those used presently in NEXT-White. NBrS is, however, discernible in the TPC buffer region of NEXT-White (i.e., between the high-voltage electrode and the ground electrodes shielding the PMT planes), and, according to our calculations, similar light levels are expected in analogous regions of liquid-based TPCs. Moreover, as argued in this work, implementation of SiPM readouts in large-volume Xe-TPCs (m^3 scale) would lead to the dominance of NBrS scintillation over S1, imposing practical limitations to the reconstruction of S1 deposits with energies below a few tens of keV.

At present, NBrS photon emission in Xe TPCs may be seen as a nuisance, at most, as it contributes to the scintillation background. Even if that would be the only implication, it would still require a detailed understanding, in particular, in the era of dark matter and coherent neutrino scattering experiments which aim to detect single photons associated to the ionization produced by nuclear recoils of very small energy. In such a regime, the single-photo-electron emission observed in the NEXT-White detector and other devices and most likely associated to NBrS could eventually mask the tiny signals associated to new physics. A clear corollary of our work is that the ample community of neutrino and dark matter experiments based on xenon should not ignore NBrS effects in their experiments. The scintillation background is an obstacle to push dark matter searches down to the low-mass limit, and future studies are required to suppress or mitigate this background for the smallest signal amplitudes.

Conversely, a deep understanding of the effect may have implications for the design of future TPCs, namely, avoiding light emission hot spots in LXe as well as high electric fields in the buffer regions, effects that have not previously been given special attention.

Lastly, the possibility of implementing a scintillation mechanism such as NBrS directly in LXe opens up intriguing possibilities toward the development of single-phase LXe TPCs based on secondary-scintillation amplification of the ionization signal, avoiding the very high electric fields required for EL production in LXe, which can eventually limit the scalability of future detectors. This could be achieved directly in the liquid using hole-type structures capable of sustaining voltages around 50–100 kV over centimeter-long distances. Despite the challenges ahead, such a technique could revolutionize the design of future neutrino and dark matter experiments.

APPENDIX: EXPERIMENTAL DATA AND UNCERTAINTIES

Table II contains a summary of the sources of statistical and systematic uncertainties of the photoelectron yield versus electric field in pure xenon as measured in this work (at 68% confidence level). The experimental results provided by the two analysis methods at low electric field values are statistically combined. Since the gas temperature and the EL gap are not accurately measured, there is a small systematic uncertainty in these values affecting both the number of detected photoelectrons and the reduced electric field. The differences between measured and simulated data obtained for the electron drift velocity (depending on E/p) and the energy deposited by alpha particles in the gas are also accounted for in the estimation of the systematic uncertainty in the number of photoelectrons. Values obtained with the waveform average method include an

additional systematic error from the photoelectron calibration of the PMT. The statistical errors assigned to the number of detected photoelectrons are estimated by varying both the 1.6-MeV energy cut and the baseline region used for offset correction. The number of detected photoelectrons obtained with the photoelectron counting method includes an additional statistical error, which is estimated by varying parameters related to the single-photoelectron peak detection, within reasonable limits. Table III includes the point-by-point uncertainties of the number of photoelectrons detected in the driftless GPSC as a function of the reduced electric field, which is the field strength normalized to the gas pressure, drift path, and number of primary ionization electrons.

TABLE II. Sources of experimental uncertainties and their typical range (at 68% confidence level).

Source of uncertainty	Relative uncertainty (%)
Temperature	1.6% (syst)
Drift length	1.0% (syst)
Deposited energy	10.5% (syst)
Drift velocity	[0.2–13.6]% (syst)
PMT photoelectron calibration (average method)	11.0% (syst)
Energy cut and baseline	[0.01–15.2]% (stat)
Single-photon detection (photon counting)	[5.0–24.0]% (stat)

TABLE III. Photon yield in pure xenon (in $ph/e^- \, cm^{-1} \, bar^-$), measured in this work as a function of the reduced electric field (in $V \, cm^- \, bar^-$). Statistical and systematic uncertainties are included. The data points correspond to the weighted average of the two experimental methods described in the text, as presented in Fig. 11. The temperature is 300 K, and the pressure is 1.24 bar. The light detection efficiency of the experimental setup is given in Fig. 13, with an estimated uncertainty of 20%.

E/p	$\sigma_{E/p}$ (syst)	Photon yield	σ_{ph} (stat)	σ_{ph} (syst)
132	2	1.12×10^{-4}	2.61×10^{-5}	1.18×10^{-5}
165	2	1.87×10^{-4}	1.11×10^{-5}	1.97×10^{-5}
199	3	3.36×10^{-4}	2.21×10^{-5}	3.70×10^{-5}
266	3	9.27×10^{-4}	4.52×10^{-5}	9.82×10^{-5}
299	4	1.47×10^{-3}	1.85×10^{-5}	1.58×10^{-4}
332	4	1.90×10^{-3}	9.15×10^{-5}	2.05×10^{-4}
399	5	2.99×10^{-3}	3.14×10^{-4}	3.54×10^{-4}
465	6	4.94×10^{-3}	5.81×10^{-5}	8.03×10^{-4}
533	7	7.17×10^{-3}	1.57×10^{-5}	1.46×10^{-3}
599	8	1.34×10^{-2}	4.09×10^{-5}	2.04×10^{-3}
667	8	3.26×10^{-2}	6.77×10^{-5}	4.96×10^{-3}
733	9	8.77×10^{-2}	5.62×10^{-5}	1.33×10^{-2}
800	10	1.99×10^{-1}	4.90×10^{-4}	3.02×10^{-2}
867	11	4.03×10^{-1}	4.91×10^{-4}	6.12×10^{-2}
934	12	6.25×10^{-1}	1.55×10^{-3}	9.50×10^{-2}
1000	13	9.14×10^{-1}	4.67×10^{-4}	1.39×10^{-1}
1068	14	1.29	4.95×10^{-3}	1.97×10^{-1}
1134	14	1.73	3.75×10^{-3}	2.63×10^{-1}
1202	15	2.08	5.90×10^{-3}	3.16×10^{-1}
1268	16	2.62	4.67×10^{-3}	3.99×10^{-1}
1335	17	2.96	3.50×10^{-3}	4.51×10^{-1}
1535	19	4.50	5.54×10^{-4}	6.84×10^{-1}
1736	22	5.54	1.19×10^{-2}	8.56×10^{-1}
1937	25	7.07	3.48×10^{-2}	1.09
2137	27	7.78	1.53×10^{-2}	1.30
2338	30	8.75	2.02×10^{-2}	1.46
2539	32	10.0	3.24×10^{-2}	1.63
2739	35	10.8	3.75×10^{-2}	1.82
2941	37	12.0	2.04×10^{-2}	2.02
3140	40	12.9	3.32×10^{-2}	2.07

[1] E. Aprile *et al.* (XENON Collaboration), *The XENON1T Dark Matter Experiment*, Eur. Phys. J. C **77**, 881 (2017).

[2] X. Cui *et al.* (PandaX-II Collaboration), *Dark Matter Results from 54-Ton-Day Exposure of PandaX-II Experiment*, Phys. Rev. Lett. **119**, 181302 (2017).

[3] D. S. Akerib *et al.* (LUX-ZEPLIN Collaboration), *Projected WIMP Sensitivity of the LUX-ZEPLIN Dark Matter Experiment*, Phys. Rev. D **101**, 052002 (2020).

[4] J. Aalbers *et al.* (DARWIN Collaboration), *DARWIN: Towards the Ultimate Dark Matter Detector*, J. Cosmol. Astropart. Phys. 11 (2016) 017.

[5] G. Mohlabeng, K. Kong, J. Li, A. Para, and J. Yoo, *Dark Matter Directionality Revisited with a High Pressure Xenon Gas Detector*, J. High Energy Phys. 07 (2015) 092.

[6] P. Ferrario *et al.* (NEXT Collaboration), *Demonstration of the Event Identification Capabilities of the NEXT-White Detector*, J. High Energy Phys. 10 (2019) 052.

[7] S. Obara *et al.* (AXEL Collaboration), *High-Pressure Xe Gas TPC for BG-Free 0ν2β Decay Search*, Nucl. Instrum. Methods Phys. Res., Sect. A **958**, 162803 (2020).

[8] J. J. Gomez-Cadenas, F. M. Capilla, and P. Ferrario, *High Pressure Gas Xenon TPCs for Double Beta Decay Searches*, Front. Phys. **7**, 51 (2019).

[9] G. Anton *et al.* (EXO-200 Collaboration), *Search for Neutrinoless Double-β Decay with the Complete EXO-200 Dataset*, Phys. Rev. Lett. **123**, 161802 (2019).

[10] K. Ni *et al.* (PandaX-II Collaboration), *Searching for Neutrino-less Double Beta Decay of* ^{136}Xe *with PandaX-II Liquid Xenon Detector*, Chin. Phys. C **43**, 113001 (2019).

[11] E. Aprile *et al.* (XENON Collaboration), *Observation of Two-Neutrino Double Electron Capture in* ^{124}Xe *with XENON1T*, Nature (London) **568**, 532 (2019).

[12] D. S. Akerib *et al.* (LUX Collaboration), *Extending Light WIMP Searches to Single Scintillation Photons in LUX*, Phys. Rev. D **101**, 042001 (2020).

[13] B. G. Lenardo *et al.*, *Low-Energy Physics Reach of Xenon Detectors for Nuclear-Recoil-Based Dark Matter and Neutrino Experiments*, Phys. Rev. Lett. **123**, 231106 (2019).

[14] M. Suzuki and S. Kubota, *Mechanism of Proportional Scintillation in Argon, Krypton and Xenon*, Nucl. Instrum. Methods **164**, 197 (1979).

[15] Y. Salamero, A. Birot, H. Brunet, H. Dijols, J. Galy, P. Millet, and J. P. Montagne, *Energy Transfer Kinetics of the VUV Emissions for Kr-Xe Mixtures*, J. Chem. Phys. **74**, 288 (1981).

[16] T. Takahashi, S. Himi, M. Suzuki, J.-Z. Ruan(Gen), and S. Kubota, *Emission Spectra from Ar-Xe, Ar-Kr, Ar-N2, Ar-CH4, Ar-CO2 and Xe-N2 Gas Scintillation Proportional Counters*, Nucl. Instrum. Methods Phys. Res. **205**, 591 (1983).

[17] V. Chepel and H. Araujo, *Liquid Noble Gas Detectors for Low Energy Particle Physics*, J. Instrum. **8**, R04001 (2013).

[18] E. Aprile and T. Doke, *Liquid Xenon Detectors for Particle Physics and Astrophysics*, Rev. Mod. Phys. **82**, 2053 (2010).

[19] K. Fujii, Y. Endo, Y. Torigoe, S. Nakamura, T. Haruyama, K. Kasami, S. Mihara, K. Saito, S. Sasaki, and H. Tawara, *High-Accuracy Measurement of the Emission Spectrum of Liquid Xenon in the Vacuum Ultraviolet Region*, Nucl. Instrum. Methods Phys. Res., Sect. A **795**, 293 (2015).

[20] E. Aprile *et al.* (XENON Collaboration), *Signal Yields of keV Electronic Recoils and Their Discrimination from Nuclear Recoils in Liquid Xenon*, Phys. Rev. D **97**, 092007 (2018).

[21] D. S. Akerib *et al.* (LUX Collaboration), *Liquid Xenon Scintillation Measurements and Pulse Shape Discrimination in the LUX Dark Matter Detector*, Phys. Rev. D **97**, 112002 (2018).

[22] E. Aprile, M. Anthony, Q. Lin, Z. Greene, P. de Perio, F. Gao, J. Howlett, G. Plante, Y. Zhang, and T. Zhu, *Simultaneous Measurement of the Light and Charge Response of Liquid Xenon to Low-Energy Nuclear Recoils at Multiple Electric Fields*, Phys. Rev. D **98**, 112003 (2018).

[23] E. Hogenbirk, J. Aalbers, P. A. Breur, M. P. Decowski, K. van Teutem, and A. P. Colijn, *Precision Measurements of the Scintillation Pulse Shape for Low-Energy Recoils in Liquid Xenon*, J. Instrum. **13**, P05016 (2018).

[24] Q. Lin, J. Fei, F. Gao, J. Hu, Y. Wei, X. Xiao, H. Wang, and K. Ni, *Scintillation and Ionization Responses of Liquid Xenon to Low Energy Electronic and Nuclear Recoils at Drift Fields from* 236 V/cm *to* 3.93 kV/cm, Phys. Rev. D **92**, 032005 (2015).

[25] S. Kubota, M. Hishida, M. Suzuki, and J. Ruan, *Liquid and Solid Argon, Krypton and Xenon Scintillators*, Nucl. Instrum. Methods Phys. Res., Sect. **196**, 101 (1982).

[26] J. Renner *et al.* (NEXT Collaboration), *Ionization and Scintillation of Nuclear Recoils in Gaseous Xenon*, Nucl. Instrum. Methods Phys. Res., Sect. A **793**, 62 (2015).

[27] V. Alvarez *et al.* (NEXT Collaboration), *Ionization and Scintillation Response of High-Pressure Xenon Gas to Alpha Particles*, J. Instrum. **8**, P05025 (2013).

[28] L. M. P. Fernandes, E. D. C. Freitas, M. Ball, J. J. Gomez-Cadenas, C. M. B. Monteiro, N. Yahlali, D. Nygren, and J. M. F. dos Santos, *Primary and Secondary Scintillation Measurements in a Xenon Gas Proportional Scintillation Counter*, J. Instrum. **5**, P09006 (2010); **5**, A12001(E) (2010).

[29] A. Takeuchi, K. Saito, Y. Kishimoto, T. Oyama, and T. Sanami, *Scintillation and Ionization Yields of Helium-Xenon Gas Mixture for Application in Neutron Detectors*, Jpn. J. Appl. Phys. **59**, 046001 (2020).

[30] Y. Nakajima, A. Goldshmidt, H. S. Matis, T. Miller, D. R. Nygren, C. A. B. Oliveira, and J. Renner, *Measurement of Scintillation and Ionization Yield with High-Pressure Gaseous Mixtures of Xe and TMA for Improved Neutrinoless Double Beta Decay and Dark Matter Searches*, J. Instrum. **11**, C03041 (2016).

[31] E. D. C. Freitas, C. M. B. Monteiro, M. Ball, J. J. Gomez-Cadenas, J. A. M. Lopes, T. Lux, F. Sanchez, and J. M. F. dos Santos, *Secondary Scintillation Yield in High-Pressure Xenon Gas for Neutrinoless Double Beta Decay (0nu beta beta) Search*, Phys. Lett. B **684**, 205 (2010).

[32] C. M. B. Monteiro, L. M. P. Fernandes, J. A. M. Lopes, L. C. C. Coelho, J. F. C. A. Veloso, J. M. F. dos Santos, K. Giboni, and E. Aprile, *Secondary Scintillation Yield in Pure Xenon*, J. Instrum. **2**, P05001 (2007).

[33] C. A. O. Henriques *et al.* (NEXT Collaboration), *Electroluminescence TPCs at the Thermal Diffusion Limit*, J. High Energy Phys. 01 (2019) 027.

[34] A. F. M. Fernandes *et al.* (NEXT Collaboration), *Low-Diffusion Xe-He Gas Mixtures for Rare-Event Detection: Electroluminescence Yield*, J. High Energy Phys. 04 (2020) 034.

[35] E. Aprile, H. Contreras, L. W. Goetzke, A. J. M. Fernandez, M. Messina, J. Naganoma, G. Plante, A. Rizzo, P. Shagin, and R. Wall, *Measurements of Proportional Scintillation and Electron Multiplication in Liquid Xenon Using Thin Wires*, J. Instrum. **9,** P11012 (2014).

[36] T. Ye, K. L. Giboni, and X. Ji, *Initial Evaluation of Proportional Scintillation in Liquid Xenon for Direct Dark Matter Detection*, J. Instrum. **9,** P12007 (2014).

[37] C. M. B. Monteiro, A. S. Conceicao, F. D. Amaro, J. M. Maia, A. C. S. S. M. Bento, L. F. R. Ferreira, J. F. C. A. Veloso, J. M. F. dos Santos, A. Breskin, and R. Chechik, *Secondary Scintillation Yield from Gaseous Micropattern Electron Multipliers in Direct Dark Matter Detection*, Phys. Lett. B **677,** 133 (2009).

[38] C. M. B. Monteiro, L. M. P. Fernandes, J. F. C. A. Veloso, C. A. B. Oliveira, and J. M. F. dos Santos, *Secondary Scintillation Yield from GEM and THGEM Gaseous Electron Multipliers for Direct Dark Matter Search*, Phys. Lett. B **714,** 18 (2012).

[39] C. Balan, E. D. C. Freitas, T. Papaevangelou, I. Giomataris, H. N. da Luz, C. M. B. Monteiro, and J. M. F. dos Santos, *Micromegas Operation in High Pressure Xenon: Charge and Scintillation Readout*, J. Instrum. **6,** P02006 (2011).

[40] S. Ban *et al.*, *Electroluminescence Collection Cell as a Readout for a High Energy Resolution Xenon Gas TPC*, Nucl. Instrum. Methods Phys. Res., Sect. A **875,** 185 (2017).

[41] D. González-Díaz, M. Fontaíña, D. García Castro, B. Mehl, R. de Oliveira, S. Williams, F. Monrabal, M. Querol, and V. Álvarez, *A New Amplification Structure for Time Projection Chambers Based on Electroluminescence*, J. Phys. Conf. Ser. **1498,** 012019 (2020).

[42] C. A. B. Oliveira, H. Schindler, R. J. Veenhof, S. Biagi, C. M. B. Monteiro, J. M. F. dos Santos, A. L. Ferreira, and J. F. C. A. Veloso, *A Simulation Toolkit for Electroluminescence Assessment in Rare Event Experiments*, Phys. Lett. B **703,** 217 (2011).

[43] C. D. R. Azevedo *et al.*, *Microscopic Simulation of Xenon-Based Optical TPCs in the Presence of Molecular Additives*, Nucl. Instrum. Methods Phys. Res., Sect. A **877,** 157 (2018).

[44] A. Buzulutskov, *Photon Emission and Atomic Collision Processes in Two-Phase Argon Doped with Xenon and Nitrogen*, Europhys. Lett. **117,** 39002 (2017).

[45] Y. A. Butikov, B. Dolgoshein, V. Lebedenko, A. Rogozhin, and B. Rodionov, *Electroluminescence of the Noble Gases*, Sov. Phys. JETP **30,** 24 (1970), http://jetp.ras.ru/cgi-bin/dn/e_030_01_0024.pdf.

[46] A. Buzulutskov, E. Shemyakina, A. Bondar, A. Dolgov, E. Frolov, V. Nosov, V. Oleynikov, L. Shekhtman, and A. Sokolov, *Revealing Neutral Bremsstrahlung in Two-Phase Argon Electroluminescence*, Astropart. Phys. **103,** 29 (2018).

[47] A. Bondar, A. Buzulutskov, A. Dolgov, E. Frolov, V. Nosov, V. Oleynikov, E. Shemyakina, and A. Sokolov, *Neutral Bremsstrahlung in Two-Phase Argon Electroluminescence: Further Studies and Possible Applications*, Nucl. Instrum. Methods Phys. Res., Sect. A **958,** 162432 (2020).

[48] T. Takeda, M. Tanaka, and K. Yorita, *Study of Luminescence Mechanism by Neutral Bremsstrahlung in Gaseous Argon*, J. Instrum. **15,** C03007 (2020).

[49] C. M. B. Monteiro, J. A. M. Lopes, J. F. C. A. Veloso, and J. M. F. dos Santos, *Secondary Scintillation Yield in Pure Argon*, Phys. Lett. B **668,** 167 (2008).

[50] A. E. Bondar, E. O. Borisova, A. F. Buzulutskov, V. V. Nosov, V. P. Oleynikov, A. V. Sokolov, and E. A. Frolov, *Effect of Neutral Bremsstrahlung on the Operation of Two-Phase Argon Detectors*, Bull. Lebedev Phys. Inst. **47,** 162 (2020).

[51] C. E. Aalseth *et al.* (DarkSide Collaboration), *SiPM-Matrix Readout of Two-Phase Argon Detectors Using Electroluminescence in the Visible and Near Infrared Range*, Eur. Phys. J. C **81,** 153 (2021).

[52] E. Aprile *et al.* (XENON100 Collaboration), *Observation and Applications of Single-Electron Charge Signals in the XENON100 Experiment*, J. Phys. G **41,** 035201 (2014).

[53] F. Monrabal *et al.* (NEXT Collaboration), *The Next White (NEW) Detector*, J. Instrum. **13,** P12010 (2018).

[54] C. A. O. Henriques *et al.* (NEXT Collaboration), *Secondary Scintillation Yield of Xenon with Sub-percent Levels of CO_2 Additive for Rare-Event Detection*, Phys. Lett. B **773,** 663 (2017).

[55] S. Geltman, *Continuum States of H$\{\hat{-}\}$ and the Free-Free Absorption Coefficient*, Astrophys. J. **141,** 376 (1965).

[56] A. Dalgarno and N. F. Lane, *Free-Free Transitions of Electrons in Gases*, Astrophys. J. **145,** 623 (1966).

[57] T. Ohmura and H. Ohmura, *Continuous Absorption due to Free-Free Transitions in Hydrogen*, Phys. Rev. **121,** 513 (1961).

[58] R. R. Johnston, *Free-Free Radiative Transitions: A Survey of Theoretical Results*, J. Quant. Spectrosc. Radiat. Transfer **7,** 815 (1967).

[59] J. Park, I. Henins, H. Herrmann, and G. Selwyn, *Neutral Bremsstrahlung Measurement in an Atmospheric-Pressure Radio Frequency Discharge*, Phys. Plasmas **7,** 3141 (2000).

[60] B. Al Atoum, S. F. Biagi, D. González-Díaz, B. J. P. Jones, and A. D. McDonald, *Electron Transport in Gaseous Detectors with a Python-Based Monte Carlo Simulation Code*, Comput. Phys. Commun. **254,** 107357 (2020).

[61] S. F. Biagi, *Monte Carlo Simulation of Electron Drift and Diffusion in Counting Gases under the Influence of Electric and Magnetic Fields*, Nucl. Instrum. Methods Phys. Res., Sect. A **421,** 234 (1999).

[62] F. E. Low, *Bremsstrahlung of Very Low-Energy Quanta in Elementary Particle Collisions*, Phys. Rev. **110,** 974 (1958).

[63] J. Martín-Albo *et al.* (NEXT Collaboration), *Sensitivity of NEXT-100 to Neutrinoless Double Beta Decay*, J. High Energy Phys. 05 (2016) 159.

[64] M. Redshaw, E. Wingfield, J. McDaniel, and E. G. Myers, *Mass and Double-Beta-Decay Q Value of Xe-136*, Phys. Rev. Lett. **98**, 053003 (2007).

[65] J. B. Albert *et al.* (EXO-200 Collaboration), *Improved Measurement of the 2νββ Half-Life of* ^{136}Xe *with the EXO-200 Detector*, Phys. Rev. C **89**, 015502 (2014).

[66] A. Gando *et al.* (KamLAND-Zen Collaboration), *Measurement of the Double-β Decay Half-Life of* ^{136}Xe *with the KamLAND-Zen Experiment*, Phys. Rev. C **85**, 045504 (2012).

[67] J. Renner *et al.* (NEXT Collaboration), *Energy Calibration of the NEXT-White Detector with 1% Resolution near* Q$_{ββ}$ *of* ^{136}Xe, J. High Energy Phys. 10 (2019) 230.

[68] P. Novella *et al.* (NEXT Collaboration), *Measurement of Radon-Induced Backgrounds in the NEXT Double Beta Decay Experiment*, J. High Energy Phys. 10 (2018) 112.

[69] G. Martínez-Lema *et al.* (NEXT Collaboration), *Calibration of the NEXT-White Detector Using* ^{83m}Kr *Decays*, J. Instrum. **13**, P10014 (2018).

[70] C. A. N. Conde and A. J. P. L. Policarpo, *A Gas Proportional Scintillation Counter*, Nucl. Instrum. Methods **53**, 7 (1967).

[71] A. J. P. L. Policarpo, M. A. F. Alves, and C. A. N. Conde, *The Argon-Nitrogen Proportional Scintillation Counter*, Nucl. Instrum. Methods **55**, 105 (1967).

[72] J. M. F. dos Santos, J. A. M. Lopes, J. F. C. A. Veloso, P. C. P. S. Simões, T. H. V. T. Dias, F. P. Santos, P. J. B. M. Rachinhas, L. F. R. Ferreira, and C. A. N. Conde, *Development of Portable Gas Proportional Scintillation Counters for X-Ray Spectrometry*, X-Ray Spectrum. **30**, 373 (2001).

[73] D. González-Díaz *et al.* (NEXT Collaboration), *Accurate γ and MeV-Electron Track Reconstruction with an Ultralow Diffusion Xenon/TMA TPC at 10 atm*, Nucl. Instrum. Methods Phys. Res., Sect. A **804**, 8 (2015).

[74] R. Luscher *et al.*, *Search for Beta Beta Decay in Xe-136: New Results from the Gotthard Experiment*, Phys. Lett. B **434**, 407 (1998).

[75] H. Qiao, C. Lu, X. Chen, K. Han, X. Ji, and S. Wang, *Signal-Background Discrimination with Convolutional Neural Networks in the PandaX-III Experiment Using MC Simulation*, Sci. Chin. Phys. Mech. Astron. **61**, 101007 (2018).

[76] E. Aprile *et al.* (XENON Collaboration), *Energy Resolution and Linearity of XENON1T in the MeV Energy Range*, Eur. Phys. J. C **80**, 785 (2020).

[77] P. Novella *et al.* (NEXT Collaboration), *Radiogenic Backgrounds in the NEXT Double Beta Decay Experiment*, J. High Energy Phys. 10 (2019) 051.

[78] SAES, Microtorr Point-of-Use Ambient Temperature Purifiers, MicroTorr MC4500-902FV cold getter, http://www.saespuregas.com/Library/specifications-brochures/MicroTorr_Brochure.pdf.

[79] J. F. Ziegler, M. D. Ziegler, and J. P. Biersack, *SRIM—The Stopping and Range of Ions in Matter (2010)*, Nucl. Instrum. Methods Phys. Res., Sect. B **268**, 1818 (2010).

[80] K. Saito, S. Sasaki, H. Tawara, T. Sanami, and E. Shibamura, *Simultaneous Measurements of Absolute Numbers of Electrons and Scintillation Photons Produced by 5.49-MeV Alpha Particles in Rare Gases*, IEEE Trans. Nucl. Sci. **50**, 2452 (2003).

[81] J. Keränen, J. Pippuri, M. Malinen, J. Ruokolainen, P. Raback, M. Lyly, and K. Tammi, *Efficient Parallel 3-d Computation of Electrical Machines with Elmer*, IEEE Trans. Magn. **51**, 1 (2015).

[82] S. J. C. do Carmo, F. I. G. M. Borges, F. L. R. Vinagre, and C. A. N. Conde, *Experimental Study of the w-Values and Fano Factors of Gaseous Xenon and Ar-Xe Mixtures for X-Rays*, IEEE Trans. Nucl. Sci. **55**, 2637 (2008).

[83] J. Allison *et al.*, *Recent Developments in Geant4*, Nucl. Instrum. Methods Phys. Res., Sect. A **835**, 186 (2016).

[84] C. H. Faham, V. M. Gehman, A. Currie, A. Dobi, P. Sorensen, and R. J. Gaitskell, *Measurements of Wavelength-Dependent Double Photoelectron Emission from Single Photons in VUV-Sensitive Photomultiplier Tubes*, J. Instrum. **10** (2015) P09010.

[85] M. Kurokawa, M. Kitajima, K. Toyoshima, T. Kishino, T. Odagiri, H. Kato, M. Hoshino, H. Tanaka, and K. Ito, *High-Resolution Total-Cross-Section Measurements for Electron Scattering from Ar, Kr, and Xe Employing a Threshold-Photoelectron Source*, Phys. Rev. A **84**, 062717 (2011).

[86] C. A. O. Henriques, Ph.D. thesis, University of Coimbra, 2019, http://hdl.handle.net/10316/87464.

[87] J. E. Velazco, J. H. Kolts, and D. W. Setser, *Rate Constants and Quenching Mechanisms for the Metastable States of Argon, Krypton, and Xenon*, J. Chem. Phys. **69**, 4357 (1978).

[88] L. Serra *et al.* (NEXT Collaboration), *An Improved Measurement of Electron-Ion Recombination in High-Pressure Xenon Gas*, J. Instrum. **10**, P03025 (2015).

[89] M. Mimura, S. Kobayashi, N. Masuyama, M. Miyajima, and N. Hasebe, *Average Numbers of Scintillation Photons and Electrons Produced by an Alpha Particle in High-Density Xenon Gas*, Jpn. J. Appl. Phys. **48**, 076501 (2009).

[90] P. Moutard, P. Laporte, J.-L. Subtil, N. Damany, and H. Damany, *Pressure Effects on Kinetics and Decay Processes in Xenon after Selective Photoexcitation*, J. Chem. Phys. **88**, 7485 (1988).

[91] J. Balamuta and M. F. Golde, *Formation of Electronically Excited Oxygen Atoms in the Reactions of Argon (3p0, 2) and Xenon (3p2) Atoms with Oxygen Molecules*, J. Phys. Chem. **86**, 2765 (1982).

[92] T. Takahashi, S. Himi, M. Suzuki, J. Ruan, and S. Kubota, *Emission Spectra from Ar-Xe, Ar-Kr,* Ar-N$_2$, Ar-CH$_4$, Ar-CO$_2$ *and* Xe-N$_2$ *Gas Scintillation Proportional Counters*, Nucl. Instrum. Methods **205**, 591 (1983).

[93] L. Baudis, M. Galloway, A. Kish, C. Marentini, and J. Wulf, *Characterisation of Silicon Photomultipliers for Liquid Xenon Detectors*, J. Instrum. **13** (2018) P10022.

[94] S. A. Kharusi *et al.* (nEXO Collaboration), technical report, 2018 [arXiv:1805.11142].

[95] F. Carnesecchi, *Light Detection in DarkSide-20k*, J. Instrum. **15** (2020) C03038.

[96] A. Parsons, T. K. Edberg, B. Sadoulet, S. Weiss, J. F. Wilkerson, K. Hurley, R. P. Lin, and G. Smith, *High Pressure Gas Scintillation Drift Chambers with Wave*

Shifter Fiber Readout, Proc. SPIE Int. Soc. Opt. Eng. **1159**, 45 (1989).

[97] B. J. Mount *et al.*, *LUX-ZEPLIN (LZ) technical design report*, 2017 [arXiv:1703.09144].

[98] G. Boyle, R. McEachran, D. Cocks, M. Brunger, S. Buckman, S. Dujko, and R. White, *Ab-Initio Electron Scattering Cross-Sections and Transport in Liquid Xenon*, J. Phys. D **49**, 355201 (2016).

[99] E. Aprile, A. Bolotnikov, A. Bolozdynya, and T. Doke, *Noble Gas Detectors* (Wiley, New York, 2007).

[100] S. E. Derenzo, T. S. Mast, H. Zaklad, and R. A. Muller, *Electron Avalanche in Liquid Xenon*, Phys. Rev. A **9**, 2582 (1974).

[101] A. Buzulutskov, *Electroluminescence and Electron Avalanching in Two-Phase Detectors*, Instruments **4**, 16 (2020).

[102] P. Juyal, K.-L. Giboni, X.-D. Ji, and J.-L. Liu, *On Proportional Scintillation in Very Large Liquid Xenon Detectors*, Nucl. Sci. Tech. **31**, 93 (2020).

[103] F. Bay, C. Cantini, S. Murphy, F. Resnati, A. Rubbia, F. Sergiampietri, and S. Wu, *Evidence of Electric Breakdown Induced by Bubbles in Liquid Argon*, technical report, 2014 [arXiv:1401.2777].

[104] M. Kuźniak *et al.*, *Development of Very-Thick Transparent GEMs with Wavelength-Shifting Capability for Noble Element TPCs*, Eur. Phys. J. C **81**, 609 (2021).

Correction: The 50th author originally published (S. Johnston) requested this name to be removed from the list, which was added inadvertently. The change was confirmed and then implemented.